

RECEIVED: March 8, 2024

ACCEPTED: May 16, 2024

PUBLISHED: June 18, 2024

Amplitude analysis of the $\Lambda_b^0 \rightarrow p K^- \gamma$ decay



The LHCb collaboration

E-mail: anja.beck@cern.ch

ABSTRACT: The resonant structure of the radiative decay $\Lambda_b^0 \rightarrow p K^- \gamma$ in the region of proton-kaon invariant-mass up to $2.5 \text{ GeV}/c^2$ is studied using proton-proton collision data recorded at centre-of-mass energies of 7, 8, and 13 TeV collected with the LHCb detector, corresponding to a total integrated luminosity of 9 fb^{-1} . Results are given in terms of fit and interference fractions between the different components contributing to this final state. Only Λ resonances decaying to $p K^-$ are found to be relevant, where the largest contributions stem from the $\Lambda(1520)$, $\Lambda(1600)$, $\Lambda(1800)$, and $\Lambda(1890)$ states.

KEYWORDS: Flavour Physics, Particle and Resonance Production, Rare Decay, Hadron-Hadron Scattering

ARXIV EPRINT: [2403.03710](https://arxiv.org/abs/2403.03710)

Contents

1	Introduction	1
2	Detector and selection	2
3	Invariant mass fit	4
4	Amplitude model	5
5	Amplitude fit	9
6	Systematic uncertainties	12
6.1	Amplitude model	12
6.2	Acceptance model	16
6.3	Mass fit model	16
6.4	Additional background contamination	16
6.5	Systematic uncertainty combinations	16
7	Results and conclusion	17
A	Logarithmic scale plots of $m_{\Lambda_b^0}(pK^-)$	20
B	Projections for the reduced and second best models	20
C	Couplings at the best fit point	21
D	Statistical correlations	25
	The LHCb collaboration	30

1 Introduction

Rare decays of b hadrons involving flavour-changing neutral currents, such as $b \rightarrow s\ell^+\ell^-$ and $b \rightarrow s\gamma$ transitions, are forbidden at tree level in the Standard Model and further suppressed at loop-level through the GIM mechanism. As a consequence, these decays are very sensitive to potential new particles that can enter virtually through loop-level processes or allow tree-level diagrams, affecting properties of these decays such as branching fractions and angular distributions. The measurements of these processes can probe higher energy scales than those accessible via direct searches.

Thanks to the abundant production of b baryons at the LHC, precision measurements of rare b -baryon decays have become possible for the first time. For example, the LHCb collaboration has performed tests of lepton universality using $\Lambda_b^0 \rightarrow pK^-\ell^+\ell^-$ decays¹ in the dilepton invariant-mass squared range $0.1 < q^2 < 6.0 \text{ GeV}^2/c^4$ and the pK^- invariant-mass range $m_{pK^-} < 2.6 \text{ GeV}/c^2$ [1]. Moreover, the LHCb collaboration has searched for CP violation in $\Lambda_b^0 \rightarrow pK^-\mu^+\mu^-$ decays [2] and measured the branching fraction of the $\Lambda_b^0 \rightarrow \Lambda(1520)\mu^+\mu^-$

¹The inclusion of charge-conjugate processes is implied throughout the text.

decay [3]. Direct interpretations of these results regarding models for physics beyond the Standard Model are difficult given the lack of detailed knowledge of the resonant structure of the pK^- spectrum in different regions of the dilepton invariant-mass spectrum.

An observation of the $\Lambda_b^0 \rightarrow pK^-\gamma$ decay was first reported unofficially in a thesis using Run 1 data (taken during 2011 and 2012) without giving a significance [4]. This paper presents an amplitude analysis of the $\Lambda_b^0 \rightarrow pK^-\gamma$ decay which constitutes the first official observation of this mode. This analysis measures $\Lambda_b^0 \rightarrow pK^-\gamma$ decay properties for the first time and characterises the pK^- spectrum at the photon pole of the recoiling system. Theoretical knowledge of the pK^- spectrum from Λ_b^0 decays, in particular the modelling of form factors, is limited to quark-model calculations [5, 6]. Predictions obtained from lattice QCD [7, 8], HQET [9] and dispersive bounds analyses [10] are only available for the decay via the $\Lambda(1520)$ state. The different Λ resonances in the pK^- spectrum have been studied using fixed target experiments with incident kaons [11, 12]. An amplitude analysis of $\Lambda_b^0 \rightarrow J/\psi pK^-$ decays, which led to the discovery of states compatible with pentaquarks [13], studied the pK^- spectrum from Λ_b^0 decays at the J/ψ resonance in the dimuon invariant-mass spectrum. Additionally, if the amplitudes of the $\Lambda_b^0 \rightarrow pK^-\gamma$ decay are known precisely, this measurement could constitute useful input to a future measurement of the photon polarisation, involving polarised Λ_b^0 baryons, for example from Z boson decays [14].

The $\Lambda_b^0 \rightarrow pK^-\gamma$ decay provides an opportunity to complement the knowledge of the pK^- spectrum, including unique access to heavier states with masses larger than about $2\text{ GeV}/c^2$ that cannot be accessed with $\Lambda_b^0 \rightarrow J/\psi pK^-$ decays due to the kinematic restrictions. Measurements of resonance properties are vital inputs to the theoretical description of low-energy QCD as discussed in ref. [15]. Employing data collected by the LHCb detector in pp collisions during the years 2011–2012 (Run 1) and 2015–2018 (Run 2), corresponding to an integrated luminosity of about 9 fb^{-1} , this paper presents the first amplitude analysis of $\Lambda_b^0 \rightarrow pK^-\gamma$ decays.

2 Detector and selection

The LHCb detector is a single-arm forward spectrometer covering the pseudorapidity range $2 < \eta < 5$, designed for the study of particles containing b or c quarks. The detector includes a high-precision tracking system consisting of a silicon-strip vertex detector surrounding the proton-proton interaction region, a large-area silicon-strip detector located upstream of a dipole magnet with a bending power of about 4 Tm , and three stations of silicon-strip detectors and straw drift tubes placed downstream of the magnet. The tracking system provides a measurement of the momentum of charged particles with a relative uncertainty that varies from 0.5% at low momentum to 1.0% at $200\text{ GeV}/c$. The minimum distance of a track to a primary proton-proton collision vertex (PV), the impact parameter (IP), is measured with a resolution of $(15 + 29/p_T)\mu\text{m}$, where p_T is the component of the momentum transverse to the beam, in GeV/c . Different types of charged hadrons are distinguished using information from two ring-imaging Cherenkov detectors. Photons, electrons and hadrons are identified by a calorimeter system consisting of scintillating-pad (SPD) and preshower detectors, an electromagnetic (ECAL) and a hadronic calorimeter. In addition, a muon system allows the identification of muons.

Samples of simulated events are used to optimise selection requirements and estimate the efficiencies of the signal and backgrounds. The simulated proton-proton collisions are generated using PYTHIA [16] with a specific LHCb configuration [17]. Decays of hadronic particles are described by EvtGen [18], in which final-state radiation is generated using PHOTOS [19]. The interaction of the generated particles with the detector, and its response, are implemented in the Geant4 toolkit [20] as described in ref. [21]. The $\Lambda_b^0 \rightarrow pK^-\gamma$ decay is generated uniformly in phase space without assumptions on the decay dynamics.

The online event selection is performed by a trigger [22, 23], which consists of a hardware stage, based on information from the calorimeter and muon systems, followed by a software stage, which applies a full event reconstruction. The trigger exploits the presence of a high energy photon reconstructed from clusters in the ECAL. In order to reduce background and improve the mass resolution for the Λ_b^0 and two-body invariant masses, clusters are required to have a transverse energy of $E_T > 2.5\text{--}2.96\,\text{GeV}$ in Run 1 and $E_T > 2.11\text{--}2.7\,\text{GeV}$ in Run 2, respectively, at the hardware trigger level. Moreover, the hardware trigger selects only events with fewer than 600 (450) hits in the SPD for Run 1 (2) to facilitate the reconstruction in the software trigger. In the software trigger, the candidate must contain two high- p_T hadrons that are significantly displaced from the interaction point, as well as a high- E_T photon. During Run 2, a multivariate classifier based on topological criteria complements the cut-based software trigger selection [24]. The Run 1 software trigger requires the di-hadron invariant mass, assuming both hadrons are kaons, to be below $2\,\text{GeV}/c^2$. This severely affects the shape of the efficiency as a function of the proton-kaon invariant mass, resulting in the need for separate treatment of Run 1 and Run 2. In addition to this cut in the Run 1 trigger, the large threshold for the photon energy results in low efficiency at high proton-kaon invariant mass. As a consequence, the proton-kaon invariant mass range up to $2.5\,\text{GeV}/c^2$ is considered.

The reconstructed Λ_b^0 candidate is required to have good-quality track and vertex fits. Two tracks, compatible with the kaon and proton hypotheses, are required to have an impact parameter larger than 0.1 mm, a transverse momentum larger than $1\,\text{GeV}/c$ as well as momentum larger than $5\,\text{GeV}/c$. The photon must have $E_T > 3\,\text{GeV}$. The Λ_b^0 decay vertex isolation is used to reject partially reconstructed backgrounds. Specifically, an upper limit is applied on the χ^2 increase in the Λ_b^0 decay vertex fit when adding the most compatible additional track, referred to in the following as $\Delta\chi_{\text{vtx}}^2(\Lambda_b^0)$. The Λ_b^0 momentum is further required to point back to the associated primary vertex.

Background candidates resulting from combinations of unrelated protons, kaons, and photons can be suppressed using kinematic variables. A Boosted Decision Tree classifier (BDT) [25] is trained on simulated events as signal proxy and on data candidates with $m(pK\gamma) > m_{\Lambda_b^0} + 300\,\text{MeV}/c^2$ as background proxy, to suppress combinatorial background by exploiting mainly kinematic variables. The input variables to the classifier are the momentum, pseudorapidity η , flight distance (FD), $\Delta\chi_{\text{vtx}}^2$ of the Λ_b^0 baryon, IP and p_T of the hadrons, and IP, momentum, and p_T of the proton-kaon combination. Additionally, the difference in the vertex-fit χ^2 of the PV associated with the Λ_b^0 baryon reconstructed with and without the Λ_b^0 candidate is used. A further input to the BDT in Run 2 is the isolation variable

$$I_{p_T} = \frac{p_T(\Lambda_b^0) - \sum p_T}{p_T(\Lambda_b^0) + \sum p_T} \quad (2.1)$$

for which the sum is taken over tracks that are not part of the signal candidate but are associated to the same PV and fall within a cone of half-angle $\Delta R < 1.7$ rad. The half-angle of a track is defined as $(\Delta R)^2 = (\Delta\theta)^2 + (\Delta\phi)^2$, where $\Delta\theta$ and $\Delta\phi$ are the differences in the polar and azimuthal angles of each track with respect to the Λ_b^0 candidate direction. The optimal BDT working point is determined by maximising the ratio $S/\sqrt{S+B}$, where S is the number of expected signal candidates estimated from simulation samples and B is the number of background candidates in the signal region estimated based on the background-dominated regions on either side of the Λ_b^0 peak.

Requirements on the particle identification variables decrease backgrounds stemming from misidentification. Nevertheless, a large amount of misidentified $B_s^0 \rightarrow \phi(\rightarrow K^+K^-)\gamma$ decays passes all particle identification selections and pollutes the sample. These are suppressed by vetoing candidates with a K^+K^- invariant mass, calculated by interpreting the proton candidate as a kaon, between 1.01 and 1.04 GeV/c^2 . Remaining contributions from misidentified $B_s^0 \rightarrow K^-K^+\gamma$ and $B^0 \rightarrow K^-\pi^+\gamma$ decays are estimated to contribute less than 0.5% of the signal yield and are therefore not included in the baseline model. Background stemming from photon misidentification, such as $\Lambda_b^0 \rightarrow pK^-\pi^0$ or $\Lambda_b^0 \rightarrow pK^-\eta$, is difficult to quantify due to their unknown resonant structures. Estimates using simulation samples assuming a uniform distribution in the respective phase space indicate a contamination of 1–2% relative to the signal decay. Limiting the analysis to a proton-kaon invariant mass of 2.5 GeV/c^2 removes at least the contributions from potential proton-photon and kaon-photon resonances of these backgrounds which would be the most distorting. Potential contamination from $\Xi_b^0 \rightarrow pK^-\gamma$ decays are investigated and found to be negligible. The data are checked for remaining misidentified backgrounds by applying higher thresholds to the proton and kaon particle identification selection requirements, and by comparing different two-body invariant mass distributions under various alternative mass hypotheses. This reveals misidentified $D^0 \rightarrow K^+K^-$ and $D^0 \rightarrow K^+\pi^-$ decays combined with an unrelated photon, which populate the low mass side band of the signal Λ_b^0 mass peak. A veto on these decays has a strong impact on the shape of the signal acceptance in the Dalitz plane. For this reason, the candidates are retained and treated as part of the combinatorial background. The effect of this treatment is considered as a systematic uncertainty. Partially reconstructed decays, such as $\Lambda_b^0 \rightarrow pK^{*-}(\rightarrow K^-\pi^0)\gamma$, where the pion is not reconstructed, are also a source of background, which is included in the fit to the three-body invariant-mass distribution described in the following.

3 Invariant mass fit

The three-body invariant mass distribution of the candidates fulfilling all selection criteria is shown in figure 1. An unbinned maximum-likelihood fit to these candidates is performed. Following the *sPlot* technique [26], a signal weight (*sWeight*) is assigned to each candidate to statistically disentangle the signal and background components in the subsequent amplitude analysis. The invariant mass fit is performed separately for Run 1 and Run 2, due to differences in the trigger configurations that affect the Dalitz plane distributions and hence require a separate treatment in the amplitude fit.

The signal is modelled by a double-sided Crystal-Ball [27] function comprising a Gaussian core with asymmetric tails. The tail parameters are determined using $\Lambda_b^0 \rightarrow pK^-\gamma$ simulation

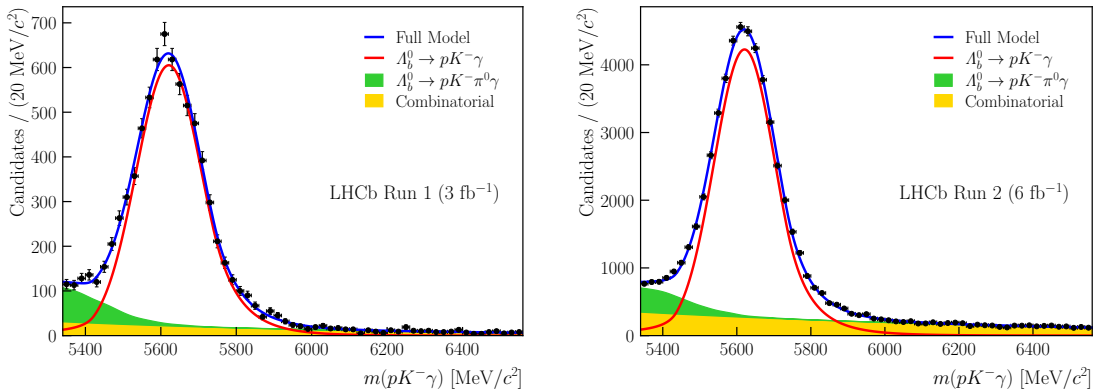


Figure 1. Distribution of the three-body invariant mass of the candidates in the (left) Run 1 and (right) Run 2 data sets. The results of the fits are overlaid.

samples. The remaining background due to random combinations of particles is modelled using a decreasing exponential function where the slope and yield are allowed to vary freely in the fit to data. The shape of the background from partially reconstructed decays is taken from simulation samples of $A_b^0 \rightarrow pK^{*-}(\rightarrow K^-\pi^0)\gamma$ decays generated uniformly in phase space, reconstructed as signal candidates, and modelled using a kernel density estimator [28] with Gaussian kernels.

Figure 1 also shows the result of the invariant-mass fits to the Run 1 and Run 2 data sets. The signal yields are determined to be 6855 ± 93 and 45558 ± 247 , in Run 1 and Run 2, respectively.

The observed width of the A_b^0 mass peak is large compared to the width reconstructed using, for example, $A_b^0 \rightarrow J/\psi pK^-$ decays [13]. This is a consequence of the large uncertainty in the photon momentum reconstruction, which is based on the ECAL cluster providing only limited directional information. Repeating the vertex fit while fixing the invariant mass of the A_b^0 candidate to the known A_b^0 mass value [29] reduces the uncertainty in the photon momentum for correctly identified $A_b^0 \rightarrow pK^-\gamma$ candidates given the excellent precision of the reconstructed proton and kaon momenta [30]. The background-subtracted data in the Dalitz plane are shown in figure 2. The two-body invariant masses displayed here, and used in the amplitude fit later, are calculated using the A_b^0 mass constraint as indicated by the A_b^0 subscript.

As a cross-check for the combination of data within a single run period, the fit to the three-body invariant mass is performed on the full data set and the data set of each year individually. No significant discrepancies between the fit results are observed. In order to validate the *sPlot* technique, fits to the three-body invariant mass are also performed in bins of the proton-kaon and the proton-photon invariant masses; these fits yield compatible results.

4 Amplitude model

The structures in the data shown in figure 2 are described using an amplitude model following the prescription of ref. [31]. The intermediate Λ resonances decaying to pK^- are modelled

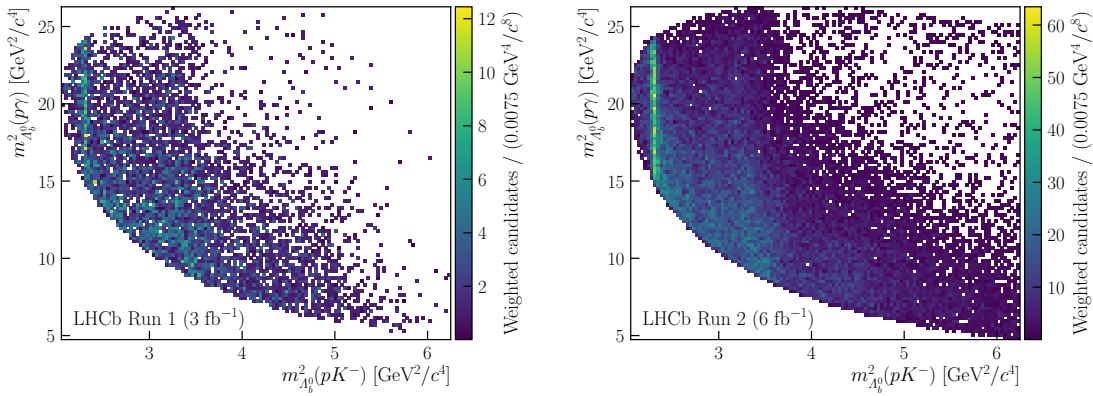


Figure 2. Distribution of the $\Lambda_b^0 \rightarrow pK^-\gamma$ candidates in the Dalitz plane, defined by $m_{\Lambda_b^0}^2(pK^-)$ and $m_{\Lambda_b^0}^2(p\gamma)$, after background-subtraction using the *sPlot* method for (left) Run 1 and (right) Run 2.

assuming Breit-Wigner lineshapes, while their spin-dependent angular distributions are described by the helicity formalism.

The three-body decay of a particle with non-zero spin results in five independent phase-space dimensions. Given that the Λ_b^0 baryons observed by LHCb are produced unpolarised [32], the dimensionality of the phase space relevant to this analysis is reduced from five to two [31]. In the following, the phase-space position is denoted \mathcal{D} . This position can be expressed in terms of the Dalitz variables [33] as shown in figure 2 for the background-subtracted data. Equivalently, the phase-space position can be given by the proton-kaon invariant mass, $m(pK^-)$ and the cosine of the proton helicity angle, $\cos\theta_p$, as is used in ref. [34]. The helicity angle of the proton, θ_p , is the polar angle of the proton momentum in the proton-kaon rest frame where the z axis coincides with the Λ resonance polarisation axis. This angle can be calculated using two steps. First, the proton and resonance momentum are boosted into the Λ_b^0 rest frame where the coordinate system is defined such that the resonance momentum direction coincides with the z axis. Second, the proton momentum is boosted into the proton-kaon rest frame. The magnitude of the z component of the obtained proton momentum, \vec{p} , defines the cosine of the proton helicity angle

$$\cos\theta_p = \frac{p_z}{|\vec{p}|}. \quad (4.1)$$

The amplitude of the decay chain $\Lambda_b^0 \rightarrow \Lambda(\rightarrow pK^-)\gamma$ with resonance spin J_Λ and particle helicities denoted by λ_i is

$$\mathcal{A}_{\lambda_\gamma, \lambda_\Lambda, \lambda_p}^A = d_{\lambda_\Lambda \lambda_p}^{J_\Lambda}(\theta_p) H_{\lambda_\Lambda, \lambda_\gamma}^A h_{\lambda_p} X_{J_\Lambda}(m(pK^-)). \quad (4.2)$$

The function $X_{J_\Lambda}(m(pK^-))$ represents the resonance dynamics. The Wigner d -matrix elements, $d_{\lambda_\Lambda \lambda_p}^{J_\Lambda}(\theta_p)$ [35], describe the rotation of spin states from the Λ helicity frame into the proton helicity frame. The helicity-coupling amplitudes H and h contain the information about the dynamics of the decays $\Lambda_b^0 \rightarrow \Lambda\gamma$ and $\Lambda \rightarrow pK^-$, respectively. Given that the kaon has spin-0, its helicity is also zero and is omitted in the index of the $\Lambda \rightarrow pK^-$ helicity amplitude, h .

Helicity conservation, defined as $\lambda_b = \lambda_A - \lambda_\gamma$, must be fulfilled. As a result, the resonance helicities can only take the values $\lambda_A = \pm\frac{1}{2}$ for $J_A = \pm\frac{1}{2}$ and $\lambda_A = \pm\frac{1}{2}, \pm\frac{3}{2}$ for $J_A \geq \frac{3}{2}$. Moreover, the resonance and photon helicities must have the same sign. Subsequently, there are two (four) helicity couplings for each resonance with spin- $\frac{1}{2}$ ($\geq \frac{3}{2}$). Standard parametrisations of resonance dynamics depend on the orbital angular momentum between the children in a decay requiring a transformation of eq. (4.2) from the helicity to the canonical basis

$$\begin{aligned} \mathcal{A}_{\lambda_\gamma, \lambda_A, \lambda_p}^A &= d_{\lambda_A \lambda_p}^{J_A}(\theta_p) \sum_{l=|J_A-s|}^{|J_A+s|} \sum_{s=|J_p-J_K|}^{|J_p+J_K|} C_{ls}^A h_{ls}^A \\ &\times \sum_{L=|J_b-S|}^{|J_b+S|} \sum_{S=|J_A-J_\gamma|}^{|J_A+J_\gamma|} C_{LS}^A H_{LS}^A X_{Ll}^A(m(pK^-)), \end{aligned} \quad (4.3)$$

where the angular dependence remains unchanged. This transformation couples the spins of the child particles in a decay to a total spin which is then coupled with their orbital angular momentum. The factors C_{LS}^A and C_{ls}^A are the products of the Clebsch-Gordan coefficients required in the spin-spin and spin-orbital-angular-momentum coupling for the resonance-photon and proton-kaon systems, respectively. In the resonance-photon system, the total spin, S , and orbital angular momentum, L , can take different values such that the product of the Clebsch-Gordan coefficients is

$$C_{LS}^A = \sqrt{\frac{2L+1}{2J_b+1}} \langle J_A, \lambda_A; J_\gamma, -\lambda_\gamma | S, (\lambda_A - \lambda_\gamma) \rangle \cdot \langle L, 0; S, (\lambda_A - \lambda_\gamma) | J_b, \lambda_b \rangle. \quad (4.4)$$

The total spin of the pK^- system is $s = \frac{1}{2}$, as the kaon carries no spin. The orbital angular momentum between the proton and the kaon, l , is fixed for a given spin-parity combination due to angular momentum and parity conservation in the strong decay $\Lambda \rightarrow pK^-$. The corresponding Clebsch-Gordan coefficients in the proton-kaon system are

$$C_{ls}^A = 1 \cdot \langle l, 0; J_p, \lambda_p | J_A, \lambda_p \rangle. \quad (4.5)$$

Hence, the summation over the spin and orbital angular momentum of the pK^- system can be dropped and only one coupling h_{ls}^A remains and is absorbed into the H_{LS}^A couplings:

$$A_{LS}^A = H_{LS}^A h_{ls}^A. \quad (4.6)$$

A standard parametrisation of resonance dynamics as employed in previous amplitude analyses (for example in refs. [13, 36]) is used:

$$X_{Ll}^A(m) = \underbrace{\left(\frac{|\vec{q}|}{q_0}\right)^L B_L(|\vec{q}|, q_0)}_{\Lambda_b^0 \rightarrow \Lambda\gamma} \underbrace{\left(\frac{|\vec{p}|}{p_0}\right)^l B_l(|\vec{p}|, p_0)}_{\Lambda \rightarrow pK^-} \text{BW}(m), \quad (4.7)$$

where \vec{q} (\vec{p}) is the momentum of the resonance (proton) in the Λ_b^0 (Λ) rest frame and B_l and B_L are Blatt-Weisskopf form factors [37]. Accordingly, the magnitudes of the momenta at

the nominal resonance mass are q_0 and p_0 . The resonance is modelled using a Breit-Wigner (BW) distribution [38]

$$\text{BW}(m) = \frac{1}{m_0^2 - m^2 - im_0\Gamma(m)}, \quad \Gamma(m) = \Gamma_0 \left(\frac{p}{p_0}\right)^{2l+1} \frac{m_0}{m} [B_l(p, p_0)]^2, \quad (4.8)$$

with resonance mass m_0 and width Γ_0 . For the $\Lambda(1405)$ resonance, with a pole-mass below the pK^- threshold, a similar approach as the amplitude analyses of $\Lambda_b^0 \rightarrow J/\psi pK^-$ [13] and $\Lambda_c^+ \rightarrow pK^-\pi^+$ [39] is employed, i.e. using a two-component width equivalent to the Flatté parametrisation [40]. The barrier factors, $(|\vec{q}|/q_0)^L$ and $(|\vec{p}|/p_0)^l$, suppress high orbital angular momenta compared to low ones, which will be exploited to simplify the model later on. The Blatt-Weisskopf form factors are equal to unity at the resonance pole and shape the resonance peak depending on the orbital angular momentum. This analysis uses the same parametrisation of the Blatt-Weisskopf functions as ref. [13]. Following the choice made in ref. [36], the radius of the Λ_b^0 baryon is taken to be $5(\text{GeV}/(c\hbar))^{-1}$ and the radius of the Λ resonances is taken to be $1.5(\text{GeV}/(c\hbar))^{-1}$.

The final decay rate is the sum over all appearing Λ resonances and their possible helicities, λ_Λ , as well as the initial and final state helicities, $\lambda_b, \lambda_\gamma, \lambda_p$

$$\frac{d\Gamma}{d\mathcal{D}} = \frac{1}{2} \sum_{\lambda_b, \lambda_\gamma, \lambda_p} \left| \sum_{\Lambda} \sum_{\lambda_\Lambda} d_{\lambda_\Lambda \lambda_p}^{J_\Lambda}(\theta_p) C_{ls}^\Lambda \sum_{L=|J_b-S|}^{|J_b+S|} \sum_{S=|J_\Lambda-J_\gamma|}^{|J_\Lambda+J_\gamma|} C_{LS}^\Lambda A_{LS}^\Lambda X_{Ll}^\Lambda (m(pK^-)) \right|^2. \quad (4.9)$$

The decay is assumed to be CP -conserving such that the amplitudes of the decay $\Lambda_b^0 \rightarrow pK^-\gamma$ and $\bar{\Lambda}_b^0 \rightarrow \bar{p}K^+\gamma$ have the same helicity couplings. As a consequence of isospin suppression, investigated experimentally in ref. [41] and theoretically in ref. [42], the $\Lambda_b^0 \rightarrow pK^-\gamma$ decay is dominated by the Λ states and therefore Σ resonances, which have the same quark content but different isospin, are not considered in this analysis. Additionally, resonances in the proton-photon and kaon-photon invariant masses are not included as they almost exclusively populate the region at $m(pK) > 2.5 \text{ GeV}/c^2$.

Besides resonances, additional nonresonant components may be necessary to achieve a satisfactory description of the data. Such nonresonant contributions are modelled similarly to the resonances, where the Breit-Wigner peak is replaced by an exponential function or a constant

$$X_{Ll}^{\text{NR,exp}}(m) = \underbrace{\left(\frac{|\vec{q}|}{q_0}\right)^L \left(\frac{|\vec{p}|}{p_0}\right)^l}_{\text{barrier factors}} \exp(-\alpha(m^2 - m_{\text{NR}}^2)),$$

$$X_{Ll}^{\text{NR,const}}(m) = \underbrace{\left(\frac{|\vec{q}|}{q_0}\right)^L \left(\frac{|\vec{p}|}{p_0}\right)^l}_{\text{barrier factors}}.$$
(4.10)

The mass parameter used in the computation of p_0 and q_0 of the nonresonant component is set to the centre of the possible proton-kaon invariant-mass range: $m_{\text{NR}} = 3.5 \text{ GeV}/c^2$. The parameter α is determined by the fit. To incorporate this into the decay rate, the sum over all resonances in eq. (4.9) needs to include the nonresonant component. The corresponding

coherent sum over the helicity states resembles the sum of a resonant contribution where only the lineshape in eq. (4.7) is replaced by the one in eq. (4.10).

Finally, the transformation into the LS basis must conserve the number of degrees of freedom (two (four) helicity couplings for each Λ with spin $\frac{1}{2}$ ($\geq \frac{3}{2}$)). However, given that the angular momentum coupling is a purely mathematical transformation and lacks physics knowledge such as $\lambda_\gamma \neq 0$, there are four (six) LS combinations for spin $\frac{1}{2}$ ($\geq \frac{3}{2}$) resonances. Translating $H_{\pm 1/2,0} = 0$ into a combination of LS couplings is non trivial. An approximation omitting all dynamical terms in eq. (4.3) is obtained by expressing the two couplings with highest S in terms of the other two or four:

$$\begin{pmatrix} A_{L_{\max},S_{\max}}^A \\ A_{L_{\max}-1,S_{\max}}^A \end{pmatrix} = - \begin{pmatrix} C_{L_{\max},S_{\max}}^+ & C_{L_{\max}-1,S_{\max}}^+ \\ C_{L_{\max},S_{\max}}^- & C_{L_{\max}-1,S_{\max}}^- \end{pmatrix}^{-1} \sum_{L,S < S_{\max}} A_{L,S}^A \begin{pmatrix} C_{LS}^+ \\ C_{LS}^- \end{pmatrix}. \quad (4.11)$$

The constants C_{LS}^\pm are the Clebsch-Gordan coefficients C_{LS}^A with resonance helicity $\lambda_\Lambda = \pm \frac{1}{2}$ and photon helicity $\lambda_\gamma = 0$. In the case of a spin- $\frac{3}{2}$ resonance for example, there are six LS combinations: $(0, \frac{1}{2}), (1, \frac{1}{2}), (1, \frac{3}{2}), (2, \frac{3}{2}), (2, \frac{5}{2}), (3, \frac{5}{2})$. The transformation in eq. (4.11) replaces the latter two and ensures that the amplitude vanishes exactly at the nominal mass of the resonance.

Two interesting quantities that can be extracted from the model are the fit fraction, the relative contribution of a single resonance to the determined full amplitude computed by

$$\text{FF}(n) = \frac{\int_{\mathcal{D}} \left(\frac{d\Gamma(n)}{d\mathcal{D}} \right) d\mathcal{D}}{\int_{\mathcal{D}} \left(\frac{d\Gamma}{d\mathcal{D}} \right) d\mathcal{D}}, \quad (4.12)$$

and the interference fit fraction

$$\text{IFF}(n, m) = \frac{\int_{\mathcal{D}} \left(\frac{d\Gamma(n,m)}{d\mathcal{D}} \right) d\mathcal{D}}{\int_{\mathcal{D}} \left(\frac{d\Gamma}{d\mathcal{D}} \right) d\mathcal{D}} - \text{FF}(n) - \text{FF}(m). \quad (4.13)$$

Here, $d\Gamma(n)/d\mathcal{D}$ is the decay rate for a single state n , i.e. where the sum in eq. (4.9) only contains the state n . Similarly, $d\Gamma(n, m)/d\mathcal{D}$ is the decay rate of two states n, m , i.e. where the sum in eq. (4.9) only contains the states n and m . In contrast, $d\Gamma/d\mathcal{D}$ is the decay rate containing all states of a given model.

5 Amplitude fit

A simultaneous, unbinned, maximum-likelihood fit of the amplitude model to the Run 1 and Run 2 data sets determines the LS couplings A_{LS} . The negative logarithm of the likelihood function (NLL) is defined as [43]

$$\text{NLL} \equiv -\log(\mathcal{L}) = - \sum_{\text{Run 1}} \log(f_1(\mathcal{D})) w_s - \sum_{\text{Run 2}} \log(f_2(\mathcal{D})) w_s. \quad (5.1)$$

The weights w_s are the *sPlot* weights presented in section 3 normalised to the effective sample size [44]. The probability distribution functions f_i correspond to the normalised rate in

eq. (4.9), multiplied by the efficiency map $\varepsilon_i(\mathcal{D})$ of Run 1 or Run 2:

$$f_i(\mathcal{D}) = \frac{\varepsilon_i(\mathcal{D})}{I_i} \frac{d\Gamma}{d\mathcal{D}}, \quad (5.2)$$

where the normalisation factor is calculated as

$$I_i = \int_{\mathcal{D}} \varepsilon_i(\mathcal{D}) \frac{d\Gamma}{d\mathcal{D}} d\mathcal{D}. \quad (5.3)$$

The efficiency maps, obtained from simulation samples, are implemented as interpolated histograms. The fit is performed using the TENSORFLOWANALYSIS package [45].

Table 1 lists all Λ resonances whose existence ranges from very likely to certain according to ref. [29]. Such states are rated three or four stars and are derived from analyses of data sets that include precision differential cross sections and polarisation observables, and are confirmed by independent analyses. The allowed values of the orbital angular momenta between the proton and the kaon, l , and the resonance and the photon, L , are given explicitly in the rightmost columns.

The fit parameters are the couplings A_{LS}^A , resulting in 45 independent complex variables when including all listed Λ resonances. A baseline fit comprising these contributions determines $\Lambda(1800)$ as the largest component. To fix the overall phase and magnitude of the full amplitude, its coupling with lowest L is therefore set to $|A_{0,1/2}^{1800}| = 1$ and $\arg(A_{0,1/2}^{1800}) = 0$.

Due to the complexity of the amplitude model, the NLL function has many local minima. Depending on the exact combination of initial values, the fit may converge to different minima. When determining the *best model*, the fit is repeated ten times starting from randomised initial values. Only the result with the lowest NLL out of these ten is compared to the other models. This procedure reduces the risk of choosing the wrong best model based on convergence to a local minimum. While the different minima correspond to different values of the couplings, the values for the fit fractions and interference fit fractions are similar for different minima. As a result of this instability with respect to the couplings, this analysis treats them as nuisance parameters while the derived fit fractions and interference fit fractions are the observables.

The quality of the fit is determined using a binned χ^2 test comparing the two-dimensional weighted data histogram in $(m_{A_b^0}(pK^-), \cos \theta_p)$ with the fit result. The latter is obtained by generating a large sample of 6×10^6 data points — more than 100 times the combined signal yield — from the fitted pdf. Because some kinematic regions are only sparsely populated, the histogram is defined using a non-uniform binning with at least 100 observed signal events in each bin. Due to the differences in the Run 1 and Run 2 acceptance shapes, this binning is calculated separately for the two subsets.

The initial model contains all well-known Λ resonances (see table 1) and no other components. This gives a good description of the major structures in the data. This model is referred to as the *reduced model*. The distribution of the proton-kaon invariant-mass in Run 1 and Run 2 is shown in figure 3. The projection of the *reduced model* including all its components is overlaid. While the *reduced model* overall describes the data spectrum well, the model is not satisfactory in the region $m_{A_b^0}(pK^-) > 2 \text{ GeV}/c^2$. As the heavy Λ states are poorly known, the mass and width of different combinations of heavy states are floated with Gaussian constraints of $100 \text{ MeV}/c^2$ around the values obtained from ref. [29] in order to

Resonance	J^P	m_0	Γ_0	Δm_0	$\Delta \Gamma_0$	σ_{m_0}	σ_{Γ_0}	l	L
$\Lambda(1405)$	$\frac{1}{2}^-$	1405	50.5	± 1.3	± 2	1.3	2	0	0, 1
$\Lambda(1520)$	$\frac{3}{2}^-$	1519	16	1518–1520	15–17	1	1	2	0, 1, 2
$\Lambda(1600)$	$\frac{1}{2}^+$	1600	200	1570–1630	150–250	30	50	1	0, 1
$\Lambda(1670)$	$\frac{1}{2}^-$	1674	30	1670–1678	25–35	4	5	0	0, 1
$\Lambda(1690)$	$\frac{3}{2}^-$	1690	70	1685–1695	50–70	5	10	2	0, 1, 2
$\Lambda(1800)$	$\frac{1}{2}^-$	1800	200	1750–1850	150–250	50	50	0	0, 1
$\Lambda(1810)$	$\frac{1}{2}^+$	1790	110	1740–1840	50–170	50	60	1	0, 1
$\Lambda(1820)$	$\frac{5}{2}^+$	1820	80	1815–1825	70–90	5	10	3	1, 2, 3
$\Lambda(1830)$	$\frac{5}{2}^-$	1825	90	1820–1830	60–120	5	30	2	1, 2, 3
$\Lambda(1890)$	$\frac{3}{2}^+$	1890	120	1870–1910	80–160	20	40	1	0, 1, 2
$\Lambda(2100)$	$\frac{7}{2}^-$	2100	200	2090–2110	100–250	10	100	4	2, 3, 4
$\Lambda(2110)$	$\frac{5}{2}^+$	2090	250	2050–2130	200–300	40	50	3	1, 2, 3
$\Lambda(2350)$	$\frac{9}{2}^+$	2350	150	2340–2370	100–250	20	100	5	3, 4, 5

Table 1. List of well-established Λ resonances and their properties as given in ref. [29]. J and P are spin and parity of the resonance. The mass m_0 and width Γ_0 correspond to the Breit-Wigner parameters and are given in MeV/c^2 and MeV respectively. The possible mass and width ranges, Δm_0 and $\Delta \Gamma_0$, are also given. If a measurement of mass and width is available, the uncertainties are given instead of a range. The columns σ_{m_0} and σ_{Γ_0} contain the σ values used to estimate the systematic uncertainty related to the resonance parameters. The rightmost columns contain the allowed values of l and L .

improve the fit quality. Allowing the mass and width of the $\Lambda(2100)$ and $\Lambda(2110)$ states to vary, while keeping those of the $\Lambda(2350)$ state fixed, yields the biggest improvement.

Another option to improve the fit quality is the addition of nonresonant contributions. The nonresonant components can affect the entire region of the phase space, and are especially important in regions where resonances with the matching spin-parity may interfere. Nonresonant components with spins up to $\frac{5}{2}$ and both parities, using an exponential or constant lineshape (see eq. (4.10)), are tested. Both lineshape functions tested yield very similar results for a given set of quantum numbers and the constant one is taken as the default lineshape. The model including a nonresonant component with quantum numbers $J^P = \frac{3}{2}^-$ results in the best fit quality for either lineshape. The fit quality of this model is better than the fit quality of the *reduced model* with floating resonance masses and widths.

As a result, the *best model* used to determine the default result consists of the *reduced model* containing all Λ states with mass and width fixed to the values given in table 1 and a nonresonant component with quantum numbers $J^P = \frac{3}{2}^-$. Figures 4 and 5 contain projections

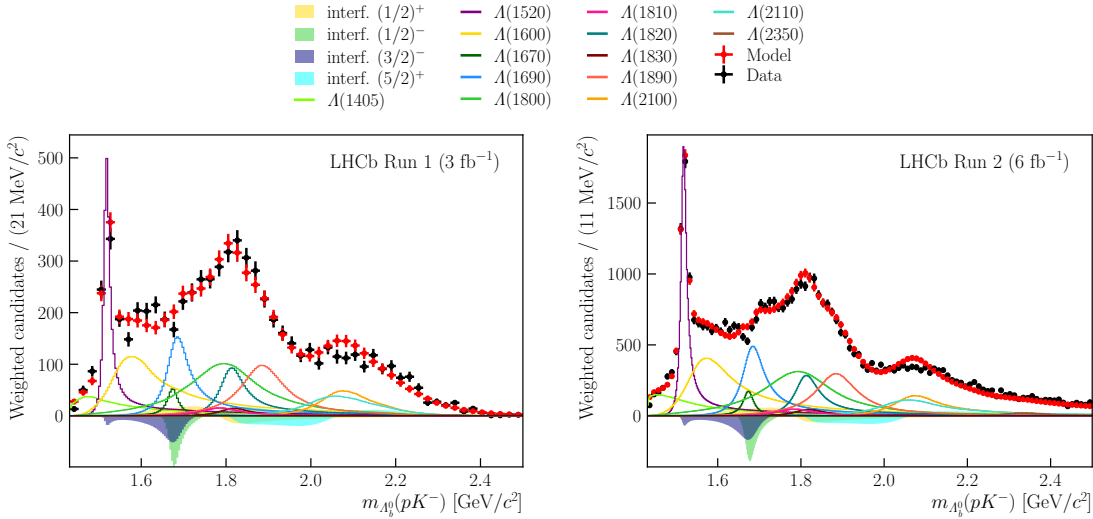


Figure 3. Background-subtracted distribution of the proton-kaon invariant-mass (black dots) for the (left) Run 1 and (right) Run 2 data samples. Also shown is a sample generated according to the result of a simultaneous fit of the *reduced model* to the data (red dots) and its components (lines) as well as the contributions due to interference between states with the same quantum numbers J^P (shaded areas).

of the data and the model with its components onto all two-body invariant masses as well as the proton helicity angle for Run 1 and Run 2. Appendix A shows the projections onto the proton-kaon invariant mass using a logarithmic vertical axis. The same set of plots is provided in appendix B for the fit with floating resonances representing the second best model.

The statistical uncertainties on the fit fractions and interference fit fractions are determined by bootstrapping the data 250 times. This means that the data set is resampled and a new set of *sWeights* is calculated from a fit to the three-body invariant mass of each bootstrap sample. Running the amplitude fit on each sample with its respective *sWeights* results in a distribution for each observable. The value for the statistical confidence interval given later is obtained by finding the shortest 68% interval around the maximum of this distribution.

6 Systematic uncertainties

Systematic uncertainties arise from four major categories: the choice of amplitude model, the acceptance model, the invariant-mass fit model, and potential remaining backgrounds. The individual uncertainties are listed in table 2 and outlined in the following.

6.1 Amplitude model

In the default fit, the masses and widths of the resonances are set to their world averages and fixed in the fit. To assess the impact of this choice, alternative masses and widths are sampled from Gaussian distributions. The widths of the Gaussians are given in table 1 as σ_{m_0} and σ_{Γ_0} and are chosen based on the ranges Δm_0 and $\Delta \Gamma_0$. Pseudoexperiments, generated using these alternative mass and width values, are fitted with the default model. The shortest 68% interval around the maximum of the distribution of the difference between the generated and fitted values is taken as a systematic uncertainty.

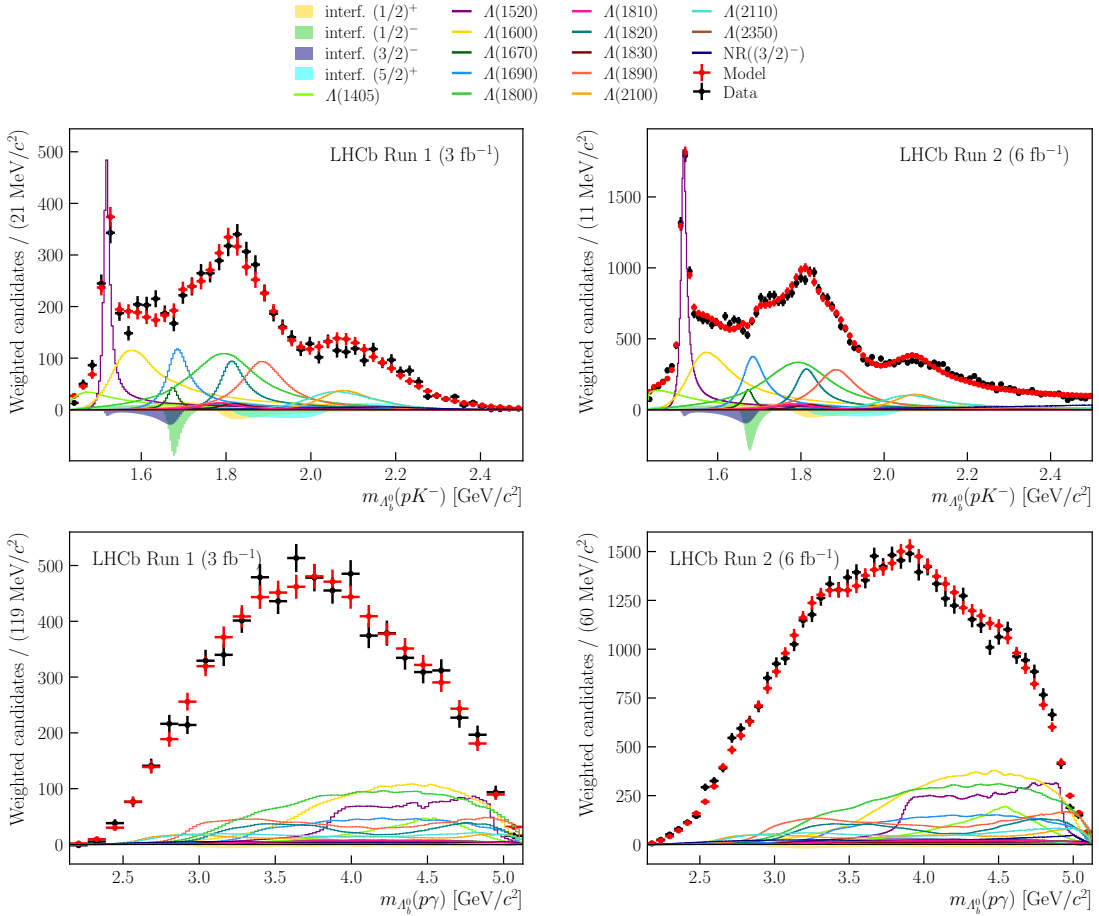


Figure 4. Background-subtracted distribution of the (top) proton-kaon and (bottom) proton-photon invariant-mass (black dots) for the (left) Run 1 and (right) Run 2 data samples. Also shown is a sample generated according to the result of a simultaneous fit of the default model to the data (red dots) and its components (lines) as well as the contributions due to interference between states with the same quantum numbers J^P (shaded areas).

Similar to the treatment of the masses and widths, also the A_b^0 and Λ radii used in the Blatt-Weisskopf functions are fixed to $d_{A_b^0} = 5 \text{ (GeV/(ch))}^{-1}$ and $d_\Lambda = 1.5 \text{ (GeV/(ch))}^{-1}$ in the default fit. The impact of this choice is assessed by generating samples with $d_{A_b^0} = 3, 5, 7 \text{ (GeV/(ch))}^{-1}$ and $d_\Lambda = 0.5, 1.5, 2.5, 3.5$ and $4.5 \text{ (GeV/(ch))}^{-1}$. These samples are fitted with the default model. The bias and standard deviation of the differences between the generated and fitted values for each combination of $d_{A_b^0}$ and d_Λ is taken as systematic uncertainty.

Besides the default model, several other models result in a good description of the data. The systematic effects due to choosing certain components and shapes over others are quantified by generating samples using an alternative model and fitting the default model to the generated pseudosample. The five alternative models are:

- removing the nonresonant component and instead floating mass and width of the $\Lambda(2100)$ and $\Lambda(2110)$ states using Gaussian constraints (this is the second best model);

Observable	Amplitude model				Acceptance model			Mass fit model		
	σ_{BW}^A	σ_{radius}^A	$\sigma_{\text{amp.}}$	$\sigma_{\text{res.}}$	σ_{finite}	$\sigma_{\text{acc.}}$	$\sigma_{\text{kin.}}$	σ_{pK}	$\sigma_{p\gamma}$	$\sigma_{\text{comb.}}$
$\Lambda(1405)$	+1.2 -0.7	+0.0 -0.0	+0.9 +0.2	+0.0 -0.4	+0.2 -0.2	+0.2 -0.2	+0.0 -0.0	+0.0 -0.1	+0.1 -0.0	+0.0 -0.0
$\Lambda(1520)$	+1.0 -1.3	+1.1 -1.1	+0.3 +0.0	+0.0 -0.1	+0.2 -0.2	+0.2 -0.2	+0.1 -0.1	+0.3 -0.0	+0.1 -0.0	+0.0 -0.1
$\Lambda(1600)$	+3.6 -4.5	+1.8 -1.8	+0.5 +0.0	+0.3 -0.2	+0.3 -0.3	+0.2 -0.2	+0.1 -0.1	+0.0 -0.1	+0.1 -0.0	+0.0 -0.0
$\Lambda(1670)$	+1.1 -0.3	+0.2 -0.2	+0.2 -0.2	+0.2 -0.2	+0.1 -0.1	+0.0 -0.0	+0.0 -0.0	+0.0 -0.0	+0.0 -0.0	+0.0 -0.0
$\Lambda(1690)$	+4.1 -0.3	+2.0 -2.0	+1.5 +0.2	+0.6 -0.5	+0.2 -0.2	+0.1 -0.1	+0.0 -0.0	+0.1 -0.0	+0.0 -0.1	+0.0 -0.0
$\Lambda(1800)$	+3.0 -5.9	+1.1 -1.1	+0.1 -0.8	+0.8 -1.5	+0.3 -0.3	+0.1 -0.1	+0.1 -0.1	+0.0 -0.0	+0.6 -0.0	+0.4 -0.0
$\Lambda(1810)$	+3.7 -0.7	+1.1 -1.1	+1.5 +0.1	+0.5 -1.4	+0.2 -0.2	+0.1 -0.1	+0.0 -0.0	+0.1 -0.0	+0.2 -0.0	+0.0 -0.0
$\Lambda(1820)$	+1.8 -4.9	+0.2 -0.2	-0.0 -0.9	+0.3 -0.4	+0.3 -0.3	+0.1 -0.1	+0.0 -0.0	+0.0 -0.3	+0.1 -0.0	+0.0 -0.1
$\Lambda(1830)$	+1.3 -0.9	+0.6 -0.6	+0.3 -0.4	+0.3 -0.5	+0.1 -0.1	+0.1 -0.1	+0.0 -0.0	+0.2 -0.0	+0.1 -0.0	+0.0 -0.0
$\Lambda(1890)$	+4.2 -5.1	+0.8 -0.8	+0.4 -0.4	+0.1 -0.4	+0.2 -0.2	+0.1 -0.1	+0.0 -0.0	+0.1 -0.0	+0.1 -0.0	+0.0 -0.0
$\Lambda(2100)$	+1.0 -2.6	+0.8 -0.8	+0.9 -0.7	+0.2 -0.2	+0.1 -0.1	+0.0 -0.0	+0.0 -0.0	+0.0 -0.0	+0.1 -0.0	+0.1 -0.0
$\Lambda(2110)$	+5.0 -0.6	+1.5 -1.5	+1.5 -0.1	+0.3 -0.2	+0.1 -0.1	+0.1 -0.1	+0.0 -0.0	+0.0 -0.2	+0.0 -0.0	+0.2 -0.0
$\Lambda(2350)$	+0.0 -0.1	+0.0 -0.0	+0.6 -0.2	+0.0 -0.0	+0.0 -0.0	+0.0 -0.0	+0.0 -0.0	+0.1 -0.0	+0.1 -0.0	+0.1 -0.0
$\text{NR}\left(\frac{3}{2}^-\right)$	+2.9 +0.3	+0.4 -0.4	+1.0 -2.4	+0.0 -0.6	+0.1 -0.1	+0.1 -0.1	+0.0 -0.0	+0.0 -0.1	+0.0 -0.3	+0.0 -0.0
$\Lambda(1405), \Lambda(1670)$	+0.4 -0.7	+0.3 -0.3	+0.2 -0.0	+0.1 -0.1	+0.1 -0.1	+0.0 -0.0	+0.0 -0.0	+0.0 -0.0	+0.0 -0.0	+0.0 -0.1
$\Lambda(1405), \Lambda(1800)$	+0.5 -3.6	+0.3 -0.3	+0.1 -1.9	+1.7 -0.4	+0.2 -0.2	+0.2 -0.2	+0.0 -0.0	+0.0 -0.0	+0.0 -0.3	+0.0 -0.0
$\Lambda(1520), \Lambda(1690)$	+0.3 -2.3	+0.9 -0.9	-0.1 -0.7	+0.5 -0.4	+0.1 -0.1	+0.0 -0.0	+0.0 -0.0	+0.0 -0.1	+0.0 -0.0	+0.0 -0.0
$\Lambda(1520), \text{NR}\left(\frac{3}{2}^-\right)$	+1.2 -2.4	+1.5 -1.5	+0.5 -0.5	+0.8 -0.4	+0.1 -0.1	+0.1 -0.1	+0.0 -0.0	+0.0 -0.0	+0.0 -0.1	+0.0 -0.0
$\Lambda(1600), \Lambda(1810)$	+4.1 -2.8	+0.6 -0.6	+1.5 -0.7	+0.9 -0.4	+0.3 -0.3	+0.2 -0.2	+0.0 -0.0	+0.0 -0.0	+0.0 -0.4	+0.0 -0.4
$\Lambda(1670), \Lambda(1800)$	+1.5 -1.9	+0.4 -0.4	+0.3 -0.2	+0.4 -0.4	+0.1 -0.1	+0.1 -0.1	+0.0 -0.0	+0.0 -0.0	+0.0 -0.0	+0.0 -0.1
$\Lambda(1690), \text{NR}\left(\frac{3}{2}^-\right)$	+0.9 -2.2	+1.1 -1.1	+0.2 -2.7	+0.2 -0.5	+0.1 -0.1	+0.1 -0.1	+0.0 -0.0	+0.0 -0.0	+0.0 -0.1	+0.0 -0.0
$\Lambda(1820), \Lambda(2110)$	+2.4 -3.1	+1.6 -1.6	+0.5 -1.6	+0.3 -0.5	+0.2 -0.2	+0.1 -0.1	+0.0 -0.0	+0.2 -0.0	+0.0 -0.3	+0.0 -0.2

Table 2. Systematic uncertainties on the fit fractions (top part of the table) and interference fit fractions (bottom part of the table). The values are given in %. The subscripts “BW”, “radius”, “amp.”, and “res.” refer to the systematic uncertainty due to fixing the resonance mass and width, fixing the radius of the hadrons, the choice of amplitude model, and the neglected resolution in the amplitude fit, respectively. The subscripts “finite”, “acc.”, and “kin.” refer to the systematic uncertainties due to the finite simulation sample used to determine the acceptance model, the choice of acceptance model, and the kinematic reweighting, respectively. The subscripts “ pK ”, “ $p\gamma$ ”, and “comb.” refer to the systematic uncertainty due to calculating the $sWeights$ in bins of the proton-kaon invariant mass, the proton-gamma invariant mass, and the choice of model for the combinatorial background in the three-body invariant mass fit respectively.

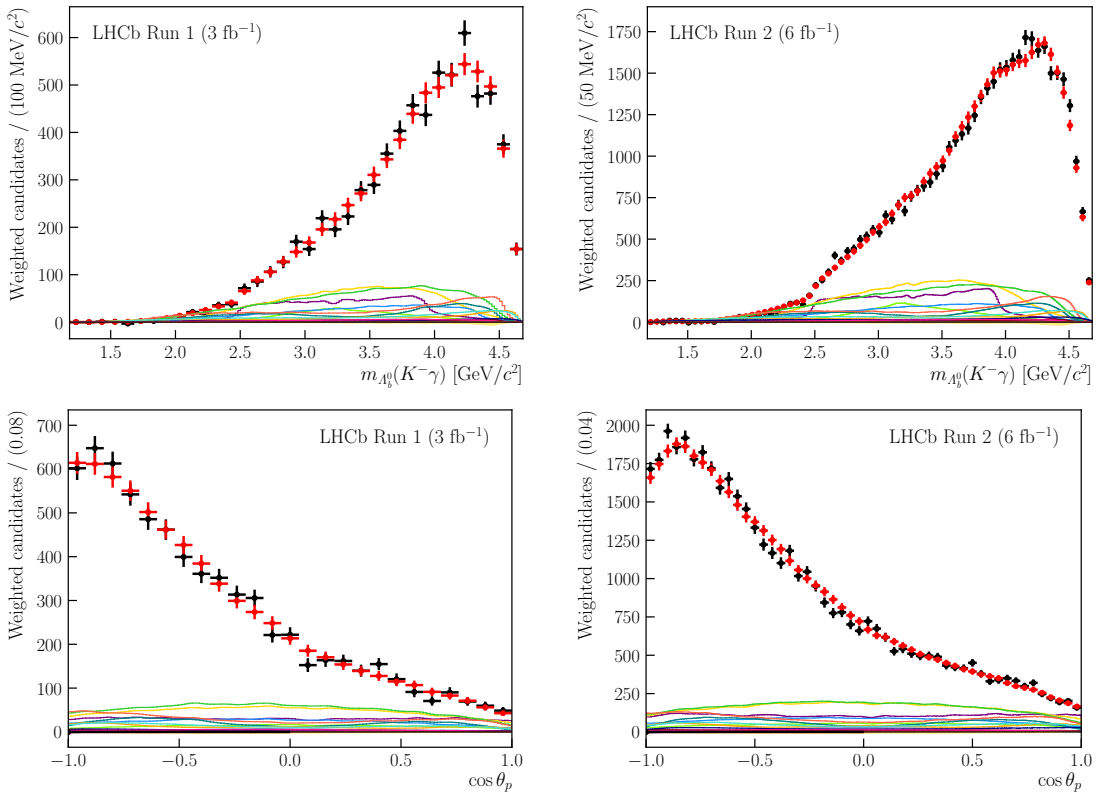


Figure 5. Background-subtracted distribution of (top) the kaon-photon invariant-mass and (bottom) the proton helicity angle (black dots) for the (left) Run 1 and (right) Run 2 data samples. Also shown is a sample generated according to the result of a simultaneous fit of the default model to the data (red dots) and its components (lines) as well as the contributions due to interference between states with the same quantum numbers J^P (shaded areas). See figure 4 for the legend.

- using an exponential function instead of a constant for the lineshape of the nonresonant component;
- employing a sub-threshold Breit-Wigner for the lineshape of the $\Lambda(1405)$ state instead of the Flatté shape;
- adding a second nonresonant component with constant lineshape and $J^P = \frac{5}{2}^+$;
- adding a second nonresonant component with constant lineshape and $J^P = \frac{1}{2}^+$.

The systematic uncertainty due to the model choices is calculated based on the mean and spread of the results obtained using the five alternative models.

Because the resolution is much smaller than the width of the resonances in all regions of the Dalitz plane, the amplitude model does not include resolution effects in the two-body invariant masses, $m_{A_b^0}(pK)$ and $m_{A_b^0}(p\gamma)$. The systematic impact of this choice is tested by generating samples with the default model and smearing the masses according to the resolution determined on simulation samples. Both the unsmeared and smeared samples are fit with the default model which does not account for the resolution. The shortest 68% interval around the maximum of the distribution of the difference between the two results is taken as a systematic uncertainty.

6.2 Acceptance model

The acceptance map is created using a simulation sample generated uniformly in phase space. The finite size of the sample, the choices regarding particle identification and kinematic modelling, as well as the number of bins in the acceptance histogram are varied individually to assess their impact on the observables. The fit to data is repeated with each alternative acceptance map and the difference between the default and alternative result calculated. The spread of the differences for the acceptance-related systematic effects, namely the finite sample size, the acceptance model, and the kinematic weights are taken as individual systematic uncertainties. The uncertainty associated with the particle identification weights is found to be negligible.

6.3 Mass fit model

In order to quantify systematic effects due to choices in the fit to the Λ_b^0 invariant mass, the analysis is performed for each of these alternatives:

- modelling the combinatorial background using a polynomial instead of an exponential function;
- modelling the partially reconstructed background using an Argus function [46] instead of a kernel density estimator obtained from simulation samples;
- letting the signal tail parameters vary in the fit to data using a Gaussian constraint instead of fixing them;
- calculating the *sWeights* in bins of $m_{\Lambda_b^0}(pK^-)$ and $m_{\Lambda_b^0}(p\gamma)$ to account for possible correlations between the Dalitz variables and the three-body invariant mass.

Only changing the shape of the combinatorial background and calculating the *sWeights* in bins of the two-body invariant masses results in a difference with respect to the default result; this difference is added as a systematic uncertainty.

6.4 Additional background contamination

After the selection, a small number of candidates from misidentified $D^0 \rightarrow K^+K^-$ and $D^0 \rightarrow K^+\pi^-$ decays combined with a random photon remain in the data sample. In the three-body invariant mass, they are predominantly located below the Λ_b^0 mass peak. The full analysis chain is repeated vetoing both D^0 decays in order to determine the systematic effect of this choice and no difference is observed.

The contamination due to misidentified $B_s^0 \rightarrow K^+K^-\gamma$ and $B^0 \rightarrow K^+\pi^-\gamma$ decays is estimated to not exceed 0.5% of the signal yield. The resulting structures are wide and spread across large parts of the phase space. Nevertheless, the two backgrounds are included in the mass fit constraining their yield to 0.5% of the signal yield. The amplitude fit is repeated using the obtained alternative set of *sWeights*. No difference to the default result is observed.

6.5 Systematic uncertainty combinations

Table 2 contains all individual systematic uncertainties considered for the final result. Sources of systematic uncertainty found to have no impact on the default values are neglected: the limited simulation sample size and the particle identification weights used to determine the

acceptance model, the shape of the signal and combinatorial background in the fit to the three-body invariant mass, and the consideration of additional misidentified B_s^0 and B^0 backgrounds in the mass fit as well as vetoing misidentified backgrounds from D^0 decays. All acceptance-related systematic uncertainties are assumed to be Gaussian and centred around the default value. All mass fit systematic uncertainties are also assumed to be Gaussian and centred around the default value, however only allowing values on either the positive or negative side as the nature of these systematic effects is a one-sided bias instead of a double-sided uncertainty. The systematic uncertainty related to the amplitude model is considered to be Gaussian but biased with respect to the default value. Similarly to the statistical uncertainty, the systematic uncertainty due to fixing the resonance parameters and neglecting the resolution are neither centred around the default value nor symmetric.

As a consequence of asymmetric non-Gaussian behaviour of these distributions, the uncertainties can not be combined by taking the square root of the sum of the individual uncertainties squared. Instead, they are combined by numerically convolving the distributions and taking the shortest 68% interval around the maximum of the resulting distribution as the combined uncertainty interval. The uncertainty due to the poorly known Λ resonance parameters dominates the combination. In order to differentiate between the uncertainty due to this external input and the systematic uncertainty related to the analysis choices, the combination is performed once for all sources of systematic uncertainty and once for all but $\sigma_{\text{BW}}^{\Lambda}$ and σ_{radius} . The two external uncertainties $\sigma_{\text{BW}}^{\Lambda}$ and $\sigma_{\text{radius}}^{\Lambda}$ are combined to give $\sigma_{\text{syst}}^{\text{external}}$.

7 Results and conclusion

The results of this analysis, including statistical and systematic uncertainties, are presented in figure 6 and table 3. The statistical correlations between the observables are given in appendix D. The data and model projections on the invariant masses and proton helicity angle are shown in figures 4 and 5. The largest resonant contributions to the $\Lambda_b^0 \rightarrow pK^-\gamma$ decay are found to arise from the $\Lambda(1800)$, $\Lambda(1600)$, $\Lambda(1890)$ and $\Lambda(1520)$ states, in decreasing order. The largest interference term involves the $\Lambda(1405)$ and $\Lambda(1800)$ baryons.

The uncertainties for most observables are dominated by external inputs, specifically the masses and widths of the Λ states. A future measurement including improved knowledge of the different Λ baryons and more data will result in a significant reduction of the uncertainties.

The analysis of $\Lambda_b^0 \rightarrow pK^-\gamma$ decays provides information about the composition of the pK^- spectrum with unique access to the heavier Λ states. A comparison between the composition of the spectrum in $\Lambda_b^0 \rightarrow pK^-\gamma$ and $\Lambda_b^0 \rightarrow J/\psi pK^-$ decays, see ref. [13], is complicated due to the different extent of the phase space and the prominent pentaquark contributions in the latter. Three notable differences are explained in the following. First, the contribution of the sub-threshold resonance $\Lambda(1405)$ is much smaller in the radiative mode. Second, the $\Lambda(1810)$ state appears small in decays to a photon but large in the J/ψ case; the neighbouring $\Lambda(1820)$ state behaves in the opposite way. This observation reveals a potential ambiguity between the two resonances also echoed in the systematic uncertainties on their fit fractions presented in this paper. Third, the heavy resonances $\Lambda(1890)$, $\Lambda(2100)$, $\Lambda(2110)$, and $\Lambda(2350)$ are much larger in the radiative case, which is in part due to the phase space enhancement.

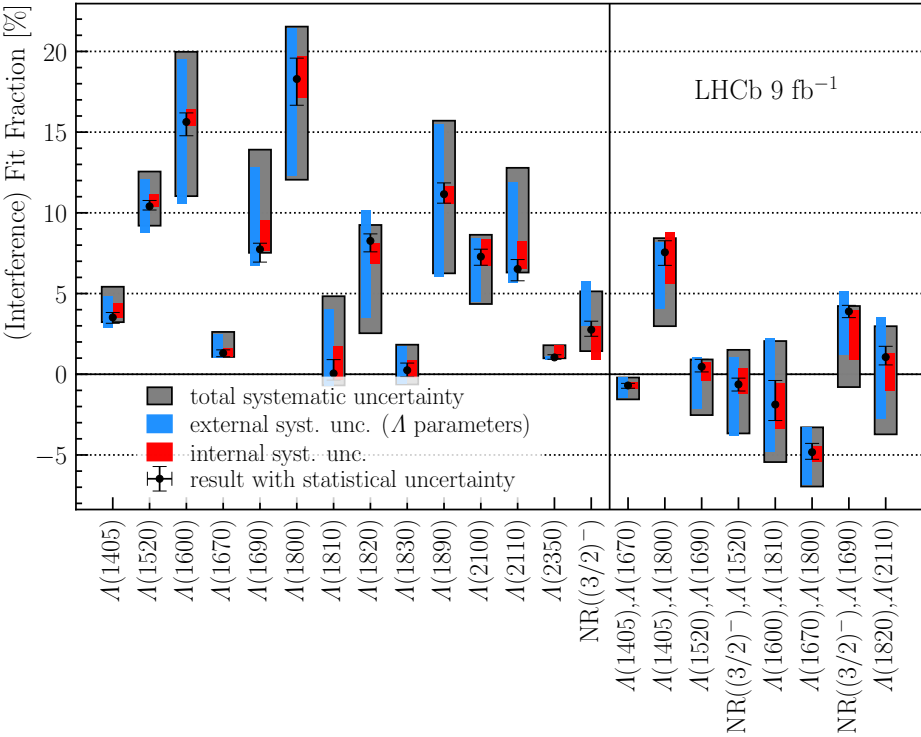


Figure 6. Final results for the fit fractions and interference fit fractions. The vertical line separates the fit from the interference fit fractions. The error bars represent the different sources of uncertainty.

In conclusion, an amplitude analysis of the decay $\Lambda_b^0 \rightarrow pK^-\gamma$ is presented for the first time, based on the helicity formalism. A sample of around 50 000 signal candidates is selected from proton-proton collisions recorded by the LHCb experiment at centre-of-mass energies of 7, 8 and 13 TeV. The default fit model comprises all known Λ resonances as well as a nonresonant contribution with quantum numbers $J^P = \frac{3}{2}^-$. The presented amplitude model provides a detailed description of the $\Lambda_b^0 \rightarrow pK^-\gamma$ decay with possible applications ranging from searches for beyond the Standard Model physics in $\Lambda_b^0 \rightarrow pK^-\ell^+\ell^-$ decays to QCD studies and a possible measurement of the photon polarisation in $\Lambda_b^0 \rightarrow pK^-\gamma$ decays using polarised Λ_b^0 baryons from Z decays at future e^+e^- colliders.

Acknowledgments

We express our gratitude to our colleagues in the CERN accelerator departments for the excellent performance of the LHC. We thank the technical and administrative staff at the LHCb institutes. We acknowledge support from CERN and from the national agencies: CAPES, CNPq, FAPERJ and FINEP (Brazil); MOST and NSFC (China); CNRS/IN2P3 (France); BMBF, DFG and MPG (Germany); INFN (Italy); NWO (The Netherlands); MNiSW and NCN (Poland); MCID/IFA (Romania); MICINN (Spain); SNSF and SER (Switzerland); NASU (Ukraine); STFC (United Kingdom); DOE NP and NSF (U.S.A.). We acknowledge the computing resources that are provided by CERN, IN2P3 (France), KIT and DESY (Germany), INFN (Italy), SURF (The Netherlands), PIC (Spain), GridPP (United Kingdom), CSCS (Switzerland), IFIN-HH (Romania), CBPF (Brazil), and Polish WLCG (Poland). We

Observable	Value	σ_{stat}	$\sigma_{\text{syst}}^{\text{internal}}$	$\sigma_{\text{syst}}^{\text{external}}$	σ_{syst}
$\Lambda(1405)$	3.5	+0.3 -0.4	+0.9 -0.0	+1.3 -0.6	+1.9 -0.3
$\Lambda(1520)$	10.4	+0.4 -0.2	+0.7 -0.0	+1.7 -1.6	+2.2 -1.2
$\Lambda(1600)$	15.6	+0.6 -0.9	+0.8 -0.2	+3.9 -5.0	+4.3 -4.6
$\Lambda(1670)$	1.3	+0.2 -0.2	+0.3 -0.2	+1.2 -0.3	+1.3 -0.2
$\Lambda(1690)$	7.7	+0.4 -0.8	+1.8 -0.1	+5.1 -1.0	+6.2 -0.2
$\Lambda(1800)$	18.3	+1.3 -1.6	+1.4 -1.1	+3.2 -6.0	+3.2 -6.2
$\Lambda(1810)$	0.1	+0.9 -0.4	+1.7 -0.4	+4.0 -0.7	+4.8 -0.7
$\Lambda(1820)$	8.3	+0.4 -0.7	-0.2 -1.4	+1.9 -4.8	+1.0 -5.7
$\Lambda(1830)$	0.3	+0.4 -0.4	+0.6 -0.5	+1.5 -0.9	+1.6 -0.9
$\Lambda(1890)$	11.2	+0.7 -0.6	+0.5 -0.6	+4.3 -5.1	+4.6 -4.9
$\Lambda(2100)$	7.3	+0.5 -0.5	+1.1 -0.6	+1.1 -2.8	+1.4 -2.9
$\Lambda(2110)$	6.5	+0.6 -0.7	+1.7 -0.0	+5.4 -0.9	+6.3 -0.2
$\Lambda(2350)$	1.0	+0.2 -0.1	+0.8 -0.0	+0.0 -0.2	+0.8 -0.1
$\text{NR}\left(\frac{3}{2}^{-}\right)$	2.8	+0.5 -0.4	+0.2 -1.9	+3.0 +0.3	+2.4 -1.3
$\Lambda(1405), \Lambda(1670)$	-0.7	+0.1 -0.2	+0.2 -0.2	+0.5 -0.8	+0.5 -0.9
$\Lambda(1405), \Lambda(1800)$	7.6	+0.7 -0.8	+1.2 -2.0	+0.6 -3.5	+0.9 -4.6
$\Lambda(1520), \Lambda(1690)$	0.5	+0.5 -0.3	+0.3 -0.9	+0.6 -2.6	+0.5 -3.0
$\Lambda(1520), \text{NR}\left(\frac{3}{2}^{-}\right)$	-0.6	+0.4 -0.4	+1.0 -0.6	+1.6 -3.2	+2.1 -3.0
$\Lambda(1600), \Lambda(1810)$	-1.9	+1.5 -1.0	+1.3 -1.5	+4.1 -2.9	+3.9 -3.6
$\Lambda(1670), \Lambda(1800)$	-4.8	+0.5 -0.4	+0.4 -0.6	+1.5 -2.0	+1.5 -2.1
$\Lambda(1690), \text{NR}\left(\frac{3}{2}^{-}\right)$	3.9	+0.4 -0.4	+0.1 -3.0	+1.2 -2.7	+0.3 -4.7
$\Lambda(1820), \Lambda(2110)$	1.1	+0.7 -0.5	+0.2 -2.1	+2.5 -3.9	+1.9 -4.8

Table 3. Fit fractions (top) and interference fit fractions (bottom) determined using the amplitude model. The values are given in %. The uncertainties from internal and external sources, determined by the numerical convolution procedure are labelled $\sigma_{\text{syst}}^{\text{internal}}$ and $\sigma_{\text{syst}}^{\text{external}}$.

are indebted to the communities behind the multiple open-source software packages on which we depend. Individual groups or members have received support from ARC and ARDC (Australia); Key Research Program of Frontier Sciences of CAS, CAS PIFI, CAS CCEPP, Fundamental Research Funds for the Central Universities, and Sci. & Tech. Program of Guangzhou (China); Minciencias (Colombia); EPLANET, Marie Skłodowska-Curie Actions,

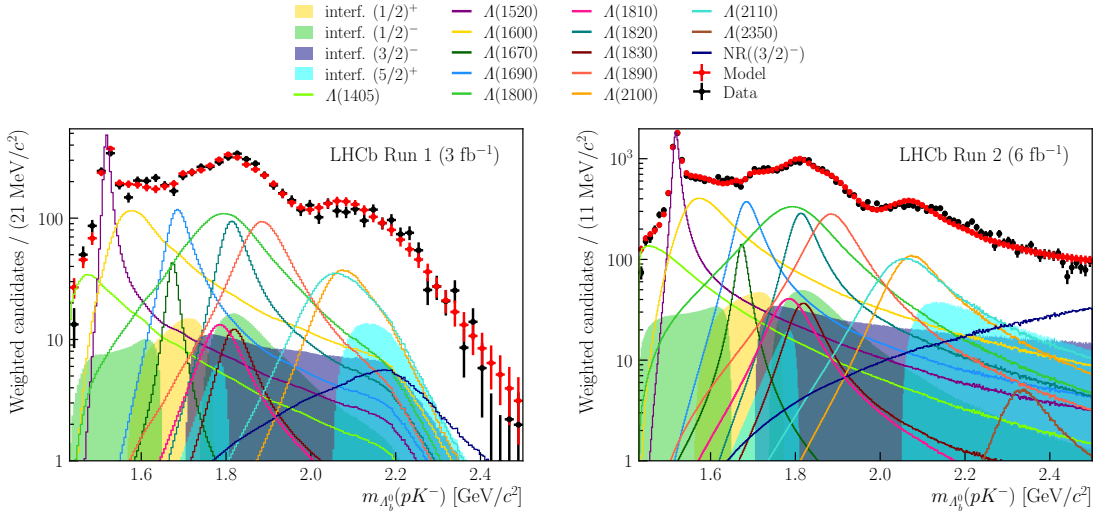


Figure 7. Background-subtracted distribution of the proton-kaon invariant-mass (black dots) for the (left) Run 1 and (right) Run 2 data samples on a logarithmic scale. Also shown is a sample generated according to the result of a simultaneous fit of the default model to the data (red dots) and its components (lines) as well as the contributions due to interference between states with the same quantum numbers J^P (shaded areas).

ERC and NextGenerationEU (European Union); A*MIDEX, ANR, IPhU and Labex P2IO, and Région Auvergne-Rhône-Alpes (France); AvH Foundation (Germany); ICSC (Italy); GVA, XuntaGal, GENCAT, Inditex, InTalent and Prog. Atracción Talento, CM (Spain); SRC (Sweden); the Leverhulme Trust, the Royal Society and UKRI (United Kingdom). A portion of this work was awarded the Martin Schmeißer Medal.

A Logarithmic scale plots of $m_{A_b^0}(pK^-)$

The plots in figure 7 are equivalent to the top plots in figure 4 with a logarithmic vertical axis in order to make all components visible. This means the plots contain the background corrected data distributions in the proton-kaon invariant mass. The plots also contain the full fit model and the individual components. Note that there are regions where the interference terms become negative but this cannot be displayed on a logarithmic scale.

B Projections for the reduced and second best models

The *reduced model* consists of the Λ resonances in table 1. The *best* and second best model are based on the *reduced model*. Contrary to the *best model*, the second best model has no nonresonant component but instead the mass and width of the $\Lambda(2100)$ and $\Lambda(2110)$ states are floated in the fit.

Figure 8 shows the fit projections on the proton-photon and kaon-photon invariant-mass, as well as the proton helicity angle for the *reduced model*. Figure 9 shows the fit projections on the two-body invariant masses and the proton helicity angle for this fit. Figures 10 and 11 show the projections on the proton-kaon invariant mass for the *reduced model* and the second best model using a logarithmic scale.

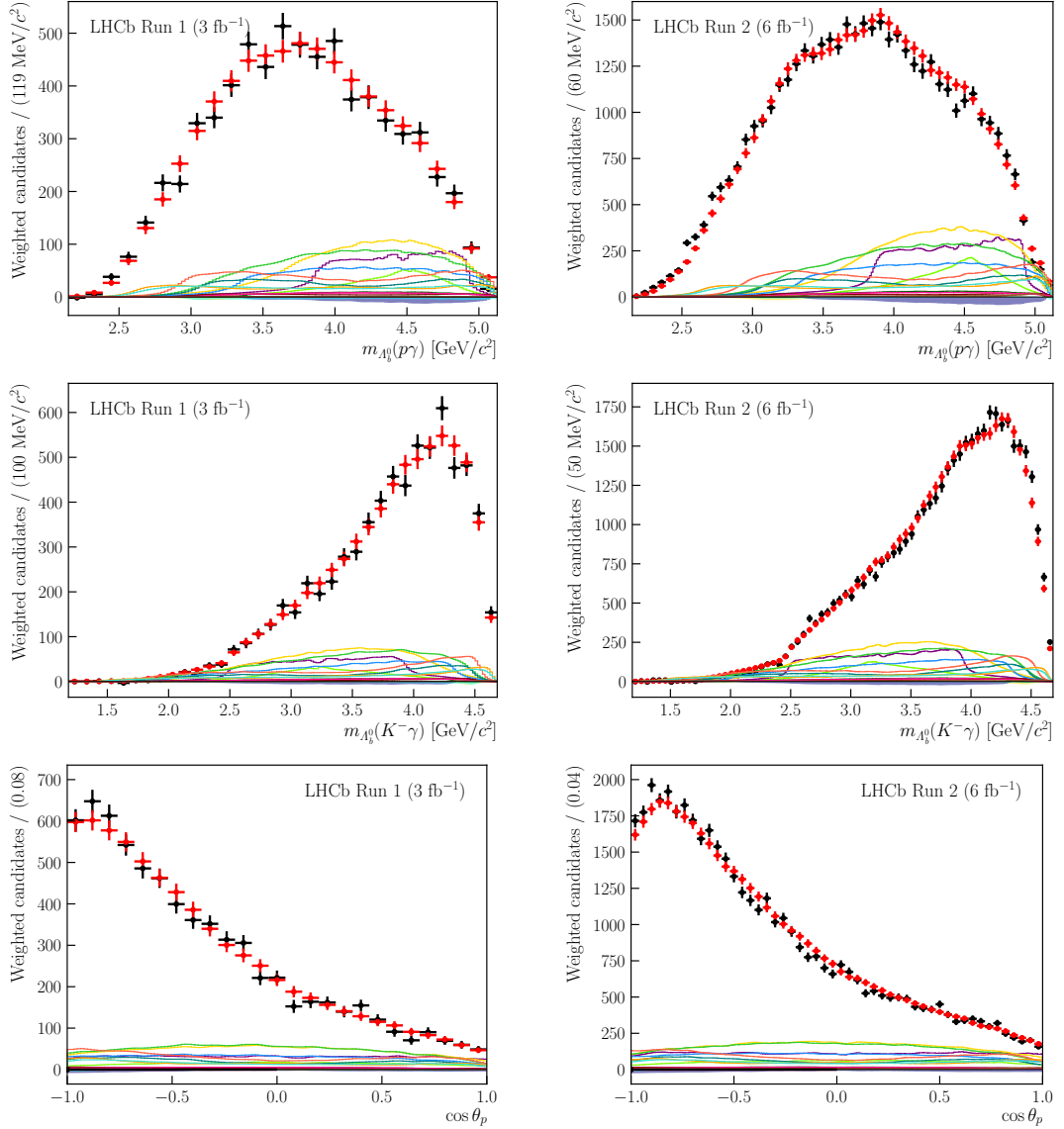


Figure 8. Background-subtracted distribution of (top) the proton-photon invariant-mass, (middle) the kaon-photon invariant-mass, and (bottom) the proton helicity angle (black dots) for the (left) Run 1 and (right) Run 2 data samples. Also shown is a sample generated according to the result of a simultaneous fit of the *reduced model* to the data (red dots) and its components (lines) as well as the contributions due to interference between states with the same quantum numbers J^P (shaded areas). See figure 3 for the legend.

C Couplings at the best fit point

Tables 4 and 5 give the value of the couplings, A_{LS} , obtained from the fit of the default model to data. These values serve primarily to construct the model and cannot be interpreted as measurements. Uncertainties for the couplings are not calculated as they generally are unstable such that minor changes (as are done when estimating systematic uncertainties) can result in very different couplings. The rightmost column indicates which couplings are dependent on the others via eq. (4.11).

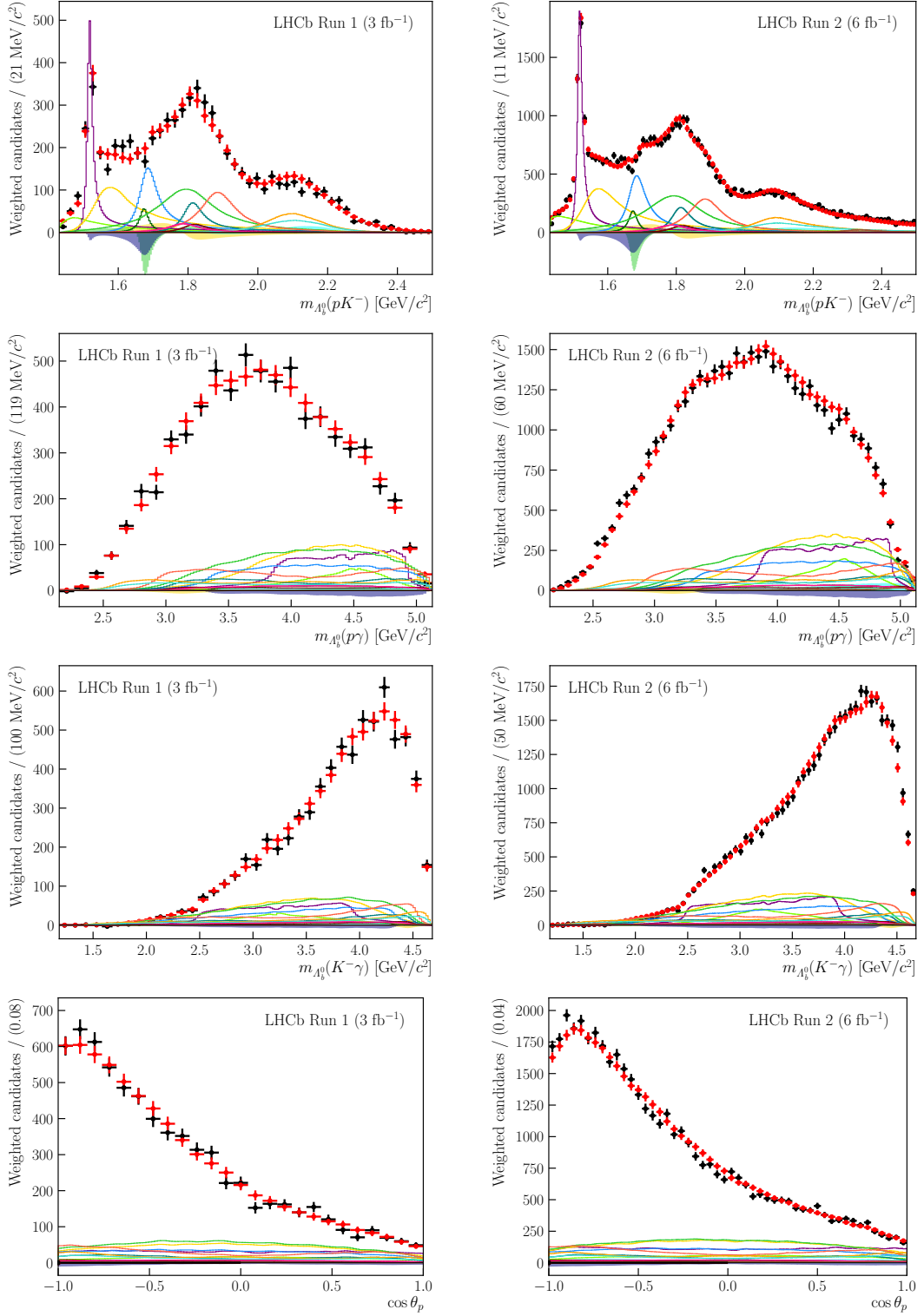


Figure 9. Background-subtracted distribution of (top three rows) the two-body invariant-masses and (bottom row) the proton helicity angle (black dots) for the (left) Run 1 and (right) Run 2 data samples. Also shown is a sample generated according to the result of a simultaneous fit of the second best model to the data (red dots) and its components (lines) as well as the contributions due to interference between states with the same quantum numbers J^P (shaded areas). See figure 3 for the legend.

Resonance	$2L$	$2S$	$ A_{LS} $	$\arg(A_{LS})$	additional comment
$\Lambda(1405)$	0	1	2.890	-0.672	
	2	1	2.137	-2.633	
	2	3	1.511	0.509	dependent via eq. (4.11)
	4	3	2.044	2.470	dependent via eq. (4.11)
$\Lambda(1520)$	0	1	0.400	-0.016	
	2	1	0.542	0.147	
	2	3	2.063	1.649	
	4	3	1.142	2.083	
	4	5	0.590	-0.607	dependent via eq. (4.11)
	6	5	0.773	-0.944	dependent via eq. (4.11)
$\Lambda(1600)$	0	1	7.000	0.970	
	2	1	4.127	3.057	
	2	3	2.918	-0.085	dependent via eq. (4.11)
	4	3	4.950	-2.171	dependent via eq. (4.11)
$\Lambda(1670)$	0	1	0.182	2.694	
	2	1	0.394	0.549	
	2	3	0.279	-2.592	dependent via eq. (4.11)
	4	3	0.129	-0.447	dependent via eq. (4.11)
$\Lambda(1690)$	0	1	0.371	-2.977	
	2	1	2.426	0.694	
	2	3	1.328	0.263	
	4	3	2.918	0.648	
	4	5	1.225	-2.599	dependent via eq. (4.11)
	6	5	1.418	0.824	dependent via eq. (4.11)
$\Lambda(1800)$	0	1	1.000	0.000	fixed in the fit
	2	1	4.418	-1.498	
	2	3	3.124	1.643	dependent via eq. (4.11)
	4	3	0.707	3.142	dependent via eq. (4.11)
$\Lambda(1810)$	0	1	1.453	-2.702	
	2	1	0.374	-1.129	
	2	3	0.264	2.012	dependent via eq. (4.11)
	4	3	1.027	0.440	dependent via eq. (4.11)
$\Lambda(1820)$	2	3	0.692	-2.965	
	4	3	3.166	-1.937	
	4	5	2.258	-1.733	
	6	5	3.023	-1.299	
	6	7	0.931	2.510	dependent via eq. (4.11)
	8	7	2.157	-1.984	dependent via eq. (4.11)

Table 4. Magnitude, $|A_{LS}|$, and phase, $\arg(A_{LS})$, of the couplings at the best fit point of the default model for resonances $\Lambda(1405)$, $\Lambda(1520)$, $\Lambda(1600)$, $\Lambda(1670)$, $\Lambda(1690)$, $\Lambda(1800)$, $\Lambda(1810)$, and $\Lambda(1820)$.

Resonance	$2L$	$2S$	$ A_{LS} $	$\arg(A_{LS})$	additional comment
$\Lambda(1830)$	2	3	0.646	2.337	
	4	3	0.881	-2.763	
	4	5	0.894	0.643	
	6	5	0.764	-2.560	
	6	7	0.536	2.018	dependent via eq. (4.11)
	8	7	0.931	-2.707	dependent via eq. (4.11)
$\Lambda(1890)$	0	1	2.070	-1.103	
	2	1	1.312	0.175	
	2	3	1.449	3.118	
	4	3	3.918	1.441	
	4	5	2.724	-1.376	dependent via eq. (4.11)
	6	5	1.455	0.109	dependent via eq. (4.11)
$\Lambda(2100)$	4	5	2.378	-0.537	
	6	5	5.087	1.139	
	6	7	3.192	1.384	
	8	7	6.932	1.924	
	8	9	3.088	-0.778	dependent via eq. (4.11)
	10	9	3.946	1.106	dependent via eq. (4.11)
$\Lambda(2110)$	2	3	2.093	2.382	
	4	3	6.217	-2.358	
	4	5	2.348	-1.664	
	6	5	6.899	-1.546	
	6	7	3.044	2.015	dependent via eq. (4.11)
	8	7	4.810	-2.427	dependent via eq. (4.11)
$\Lambda(2350)$	6	7	0.509	-1.829	
	8	7	0.670	-0.946	
	8	9	1.751	-1.344	
	10	9	0.848	-0.286	
	10	11	0.471	-2.076	dependent via eq. (4.11)
	12	11	0.396	-0.711	dependent via eq. (4.11)
$\text{NR}\left(\frac{3}{2}^{-}\right)$	0	1	1.368	0.598	
	2	1	8.811	3.131	
	2	3	7.525	-0.006	
	4	3	5.694	-2.808	
	4	5	2.895	0.426	dependent via eq. (4.11)
	6	5	9.075	3.132	dependent via eq. (4.11)

Table 5. Magnitude, $|A_{LS}|$, and phase, $\arg(A_{LS})$, of the couplings at the best fit point of the default model for resonances $\Lambda(1830)$, $\Lambda(1890)$, $\Lambda(2100)$, $\Lambda(2110)$, $\Lambda(2350)$, and the nonresonant component.

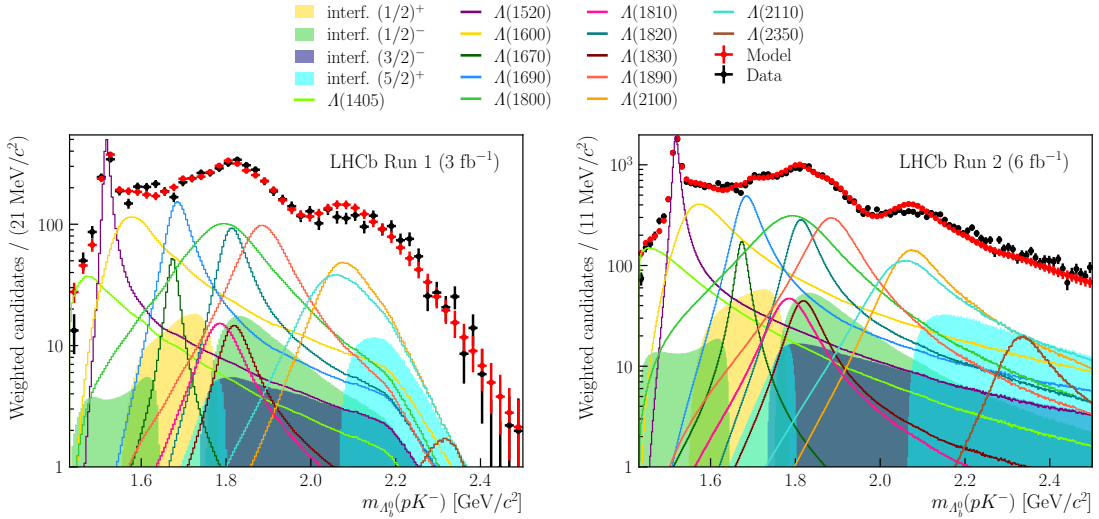


Figure 10. Background-subtracted distribution of the proton-kaon invariant-mass (black dots) for the (left) Run 1 and (right) Run 2 data samples on a logarithmic scale. Also shown is a sample generated according to the result of a simultaneous fit of the *reduced model* to the data (red dots) and its components (lines) as well as the contributions due to interference between states with the same quantum numbers J^P (shaded areas).

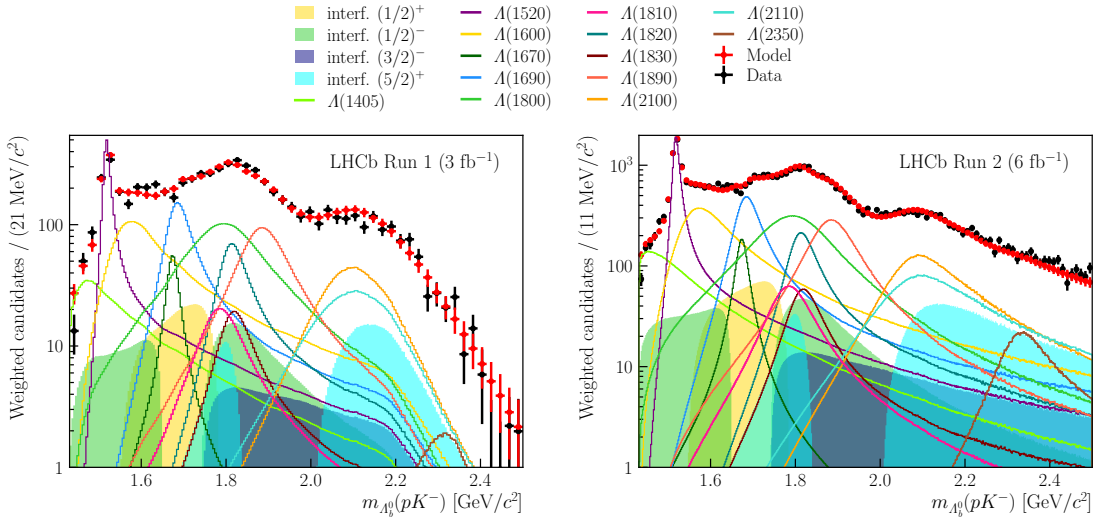


Figure 11. Background-subtracted distribution of the proton-kaon invariant-mass (black dots) for the (left) Run 1 and (right) Run 2 data samples on a logarithmic scale. Also shown is a sample generated according to the result of a simultaneous fit of the second best model to the data (red dots) and its components (lines) as well as the contributions due to interference between states with the same quantum numbers J^P (shaded areas).

D Statistical correlations

Table 6 provides the statistical correlations between the observables.

	1405	1405	1405	1520	1600	1670	1690	1800	1810	1820	1830	1890	20100	2110	2350	NR	1405, 1670	1520, 1690	1405, 1800	1670, 1800	1600, 1810	1820, 2110	1520, NR	1690, NR
1405	100																							
1520	8	100																						
1600	11	-14	100																					
1670	-37	-9	-33	100																				
1690	-7	25	-33	30	100																			
1800	-24	-13	-8	34	14	100																		
1810	21	-3	13	-20	-31	-41	100																	
1820	2	3	2	3	6	-11	3	100																
1830	16	20	-8	-20	-27	-36	33	-11	100															
1890	-3	4	11	-3	-25	-33	50	1	14	100														
2100	-21	-14	-16	21	-24	-0	8	9	28	3	100													
2110	-10	20	-5	-9	-2	27	15	-3	-9	23	-26	100												
2350	-10	-14	-15	14	4	36	14	-14	-12	-4	-3	19	100											
NR	5	7	-9	-6	-36	-2	7	-28	28	3	4	5	9	100										
1405, 1670	15	5	47	-52	-7	-19	-5	-6	-5	-8	-31	-20	-21	-23	100									
1520, 1690	-2	-11	34	-11	-53	-26	5	2	17	2	22	-28	-18	2	36	100								
1405, 1800	-40	-13	-45	18	10	-11	-15	-11	6	-9	26	-8	12	16	-34	2	100							
1670, 1800	45	14	26	-93	-27	-58	36	2	26	11	-19	2	-17	2	44	12	-20	100						
1600, 1810	-3	-3	-16	5	21	-0	-66	-18	-39	-35	-30	-22	-32	-13	20	-13	-9	-4	100					
1820, 2110	22	-18	2	-3	5	-37	-12	-5	11	-34	2	-73	-31	-16	19	20	1	12	31	100				
1520, NR	8	-6	-6	1	2	-39	45	-5	9	20	-21	-6	6	-22	-8	-7	-4	16	-12	19	100			
1690, NR	-17	-28	-12	17	9	-5	-31	2	-22	-33	2	-54	-3	-8	14	12	13	-14	40	35	-15	100		

Table 6. Statistical correlations between the observables in percent obtained from bootstrapping the data. In the interest of space, the J^P specification of the nonresonant component of the best model, NR $\left(\frac{3}{2}^-\right)$, is dropped and the resonances are only referred to by their mass. A single mass refers to the fit fraction of a state, two masses refer to the interference fit fraction of the given combination.

Open Access. This article is distributed under the terms of the Creative Commons Attribution License ([CC-BY4.0](#)), which permits any use, distribution and reproduction in any medium, provided the original author(s) and source are credited.

References

- [1] LHCb collaboration, *Test of lepton universality with $\Lambda_b^0 \rightarrow pK^-\ell^+\ell^-$ decays*, *JHEP* **05** (2020) 040 [[LHCb-PAPER-2019-040](#)] [[CERN-EP-2019-272](#)] [[arXiv:1912.08139](#)] [[INSPIRE](#)].
- [2] LHCb collaboration, *Observation of the decay $\Lambda_b^0 \rightarrow pK^-\mu^+\mu^-$ and a search for CP violation*, *JHEP* **06** (2017) 108 [[LHCb-PAPER-2016-059](#)] [[CERN-EP-2017-032](#)] [[arXiv:1703.00256](#)] [[INSPIRE](#)].
- [3] LHCb collaboration, *Measurement of the $\Lambda_b^0 \rightarrow \Lambda(1520)\mu^+\mu^-$ Differential Branching Fraction*, *Phys. Rev. Lett.* **131** (2023) 151801 [[LHCb-PAPER-2022-050](#)] [[CERN-EP-2023-007](#)] [[arXiv:2302.08262](#)] [[INSPIRE](#)].
- [4] V.J. Rives Molina, *Study of b-hadron decays into two hadrons and a photon at LHCb and first observation of b-baryon radiative decays*, Ph.D. Thesis, University of Barcelona, Barcelona, Spain (2016).
- [5] L. Mott and W. Roberts, *Rare dileptonic decays of Λ_b in a quark model*, *Int. J. Mod. Phys. A* **27** (2012) 1250016 [[arXiv:1108.6129](#)] [[INSPIRE](#)].
- [6] L. Mott and W. Roberts, *Lepton polarization asymmetries for FCNC decays of the Λ_b baryon*, *Int. J. Mod. Phys. A* **30** (2015) 1550172 [[arXiv:1506.04106](#)] [[INSPIRE](#)].
- [7] S. Meinel and G. Rendon, $\Lambda_b \rightarrow \Lambda^*(1520)\ell^+\ell^-$ form factors from lattice QCD, *Phys. Rev. D* **103** (2021) 074505 [[arXiv:2009.09313](#)] [[INSPIRE](#)].
- [8] S. Meinel and G. Rendon, $\Lambda_c \rightarrow \Lambda^*(1520)$ form factors from lattice QCD and improved analysis of the $\Lambda_b \rightarrow \Lambda^*(1520)$ and $\Lambda_b \rightarrow \Lambda_c^*(2595, 2625)$ form factors, *Phys. Rev. D* **105** (2022) 054511 [[arXiv:2107.13140](#)] [[INSPIRE](#)].
- [9] M. Bordone, *Heavy Quark Expansion of $\Lambda_b \rightarrow \Lambda^*(1520)$ Form Factors beyond Leading Order*, *Symmetry* **13** (2021) 531 [[arXiv:2101.12028](#)] [[INSPIRE](#)].
- [10] Y. Amhis, M. Bordone and M. Reboud, *Dispersive analysis of $\Lambda_b \rightarrow \Lambda(1520)$ local form factors*, *JHEP* **02** (2023) 010 [[arXiv:2208.08937](#)] [[INSPIRE](#)].
- [11] A.V. Sarantsev, M. Matveev, V.A. Nikonov, A.V. Anisovich, U. Thoma and E. Klempt, *Hyperon. Part II. Properties of excited hyperons*, *Eur. Phys. J. A* **55** (2019) 180 [[arXiv:1907.13387](#)] [[INSPIRE](#)].
- [12] M. Matveev, A.V. Sarantsev, V.A. Nikonov, A.V. Anisovich, U. Thoma and E. Klempt, *Hyperon. Part I. Partial-wave amplitudes for K^-p scattering*, *Eur. Phys. J. A* **55** (2019) 179 [[arXiv:1907.03645](#)] [[INSPIRE](#)].
- [13] LHCb collaboration, *Observation of $J/\psi p$ Resonances Consistent with Pentaquark States in $\Lambda_b^0 \rightarrow J/\psi K^-p$ Decays*, *Phys. Rev. Lett.* **115** (2015) 072001 [[LHCb-PAPER-2015-029](#)] [[CERN-PH-EP-2015-153](#)] [[arXiv:1507.03414](#)] [[INSPIRE](#)].
- [14] G. Hiller, M. Knecht, F. Legger and T. Schietinger, *Photon polarization from helicity suppression in radiative decays of polarized Λ_b to spin-3/2 baryons*, *Phys. Lett. B* **649** (2007) 152 [[hep-ph/0702191](#)] [[INSPIRE](#)].
- [15] M.F.M. Lutz et al., *Resonances in QCD*, *Nucl. Phys. A* **948** (2016) 93 [[arXiv:1511.09353](#)] [[INSPIRE](#)].

- [16] T. Sjöstrand, S. Mrenna and P.Z. Skands, *A Brief Introduction to PYTHIA 8.1*, *Comput. Phys. Commun.* **178** (2008) 852 [[arXiv:0710.3820](#)] [[INSPIRE](#)].
- [17] I. Belyaev et al., *Handling of the generation of primary events in Gauss, the LHCb simulation framework*, *J. Phys. Conf. Ser.* **331** (2011) 032047 [[INSPIRE](#)].
- [18] D.J. Lange, *The EvtGen particle decay simulation package*, *Nucl. Instrum. Meth. A* **462** (2001) 152 [[INSPIRE](#)].
- [19] N. Davidson, T. Przedzinski and Z. Was, *PHOTOS interface in C++: Technical and Physics Documentation*, *Comput. Phys. Commun.* **199** (2016) 86 [[arXiv:1011.0937](#)] [[INSPIRE](#)].
- [20] GEANT4 collaboration, *GEANT4 — a simulation toolkit*, *Nucl. Instrum. Meth. A* **506** (2003) 250 [[INSPIRE](#)].
- [21] J. Allison et al., *Geant4 developments and applications*, *IEEE Trans. Nucl. Sci.* **53** (2006) 270 [[INSPIRE](#)].
- [22] R. Aaij et al., *The LHCb Trigger and its Performance in 2011, 2013* *JINST* **8** P04022 [[arXiv:1211.3055](#)] [[INSPIRE](#)].
- [23] R. Aaij et al., *Design and performance of the LHCb trigger and full real-time reconstruction in Run 2 of the LHC*, *2019 JINST* **14** P04013 [[arXiv:1812.10790](#)] [[INSPIRE](#)].
- [24] T. Likhomanenko et al., *LHCb Topological Trigger Reoptimization*, *J. Phys. Conf. Ser.* **664** (2015) 082025 [[arXiv:1510.00572](#)] [[INSPIRE](#)].
- [25] L. Breiman, J. Friedman, R.A. Olshen and C.J. Stone, *Classification and regression trees*, Chapman and Hall/CRC (1984) [[INSPIRE](#)].
- [26] M. Pivk and F.R. Le Diberder, *SPlot: A Statistical tool to unfold data distributions*, *Nucl. Instrum. Meth. A* **555** (2005) 356 [[physics/0402083](#)] [[INSPIRE](#)].
- [27] M.J. Oreglia, *A study of the reactions $\psi' \rightarrow \gamma\gamma\psi$* , Ph.D. Thesis, Stanford University, Stanford, CA, U.S.A. (1980).
- [28] M. Rosenblatt, *Remarks on Some Nonparametric Estimates of a Density Function*, *Ann. Math. Stat.* **27** (1956) 832.
- [29] PARTICLE DATA collaboration, *Review of Particle Physics*, *Prog. Theor. Exp. Phys.* **2022** (2022) 083C01 [[INSPIRE](#)], <http://pdg.lbl.gov/>.
- [30] W.D. Hulsbergen, *Decay chain fitting with a Kalman filter*, *Nucl. Instrum. Meth. A* **552** (2005) 566 [[physics/0503191](#)] [[INSPIRE](#)].
- [31] J. Albrecht, Y. Amhis, A. Beck and C. Marin Benito, *Towards an amplitude analysis of the decay $\Lambda_b^0 \rightarrow pK^-\gamma$* , *JHEP* **06** (2020) 116 [[arXiv:2002.02692](#)] [[INSPIRE](#)].
- [32] LHCb collaboration, *Measurement of the $\Lambda_b^0 \rightarrow J/\psi\Lambda$ angular distribution and the Λ_b^0 polarisation in pp collisions*, *JHEP* **06** (2020) 110 [LHCb-PAPER-2020-005] [CERN-EP-2020-051] [[arXiv:2004.10563](#)] [[INSPIRE](#)].
- [33] R.H. Dalitz, *On the analysis of τ -meson data and the nature of the τ -meson*, *Lond. Edinb. Dubl. Phil. Mag. J. Sci.* **44** (1953) 1068 [[INSPIRE](#)].
- [34] BABAR collaboration, *An amplitude analysis of the decay $B^\pm \rightarrow \pi^\pm\pi^\pm\pi^\mp$* , *Phys. Rev. D* **72** (2005) 052002 [[hep-ex/0507025](#)] [[INSPIRE](#)].
- [35] E.P. Wigner, *Group theory and its application to the quantum mechanics of atomic spectra*, Academic Press, New York, NY, U.S.A. (1959).

- [36] LHCb collaboration, *Study of the $D^0 p$ amplitude in $\Lambda_b^0 \rightarrow D^0 p \pi^-$ decays*, *JHEP* **05** (2017) 030 [LHCb-PAPER-2016-061] [CERN-EP-2017-007] [[arXiv:1701.07873](#)] [[INSPIRE](#)].
- [37] J.M. Blatt and V.F. Weisskopf, *Theoretical nuclear physics*, Springer, New York, NY, U.S.A. (1952) [[DOI:10.1007/978-1-4612-9959-2](#)] [[INSPIRE](#)].
- [38] G. Breit and E. Wigner, *Capture of Slow Neutrons*, *Phys. Rev.* **49** (1936) 519 [[INSPIRE](#)].
- [39] LHCb collaboration, *Amplitude analysis of the $\Lambda_c^+ \rightarrow p K^- \pi^+$ decay and Λ_c^+ baryon polarization measurement in semileptonic beauty hadron decays*, *Phys. Rev. D* **108** (2023) 012023 [LHCb-PAPER-2022-002] [CERN-EP-2022-124] [[arXiv:2208.03262](#)] [[INSPIRE](#)].
- [40] S.M. Flatté, *Coupled-Channel Analysis of the $\pi\eta$ and $K\bar{K}$ Systems Near $K\bar{K}$ Threshold*, *Phys. Lett. B* **63** (1976) 224 [[INSPIRE](#)].
- [41] LHCb collaboration, *Isospin amplitudes in $\Lambda_b^0 \rightarrow J/\psi \Lambda(\Sigma^0)$ and $\Xi_b^0 \rightarrow J/\psi \Xi^0(\Lambda)$ decays*, *Phys. Rev. Lett.* **124** (2020) 111802 [LHCb-PAPER-2019-039] [CERN-EP-2019-268] [[arXiv:1912.02110](#)] [[INSPIRE](#)].
- [42] A. Dery, M. Ghosh, Y. Grossman and S. Schacht, *SU(3)_F analysis for beauty baryon decays*, *JHEP* **03** (2020) 165 [[arXiv:2001.05397](#)] [[INSPIRE](#)].
- [43] Y. Xie, *sFit: a method for background subtraction in maximum likelihood fit*, [arXiv:0905.0724](#) [[INSPIRE](#)].
- [44] C. Langenbruch, *Parameter uncertainties in weighted unbinned maximum likelihood fits*, *Eur. Phys. J. C* **82** (2022) 393 [[arXiv:1911.01303](#)] [[INSPIRE](#)].
- [45] A. Morris, *Using TensorFlow for amplitude fits — the TensorFlowAnalysis package*, Zenodo (2018) [[DOI:10.5281/zenodo.1415413](#)].
- [46] ARGUS collaboration, *Search for Hadronic $b \rightarrow u$ Decays*, *Phys. Lett. B* **241** (1990) 278 [[INSPIRE](#)].

The LHCb collaboration

- R. Aaij ³⁵, A.S.W. Abdelmotteleb ⁵⁴, C. Abellan Beteta⁴⁸, F. Abudinén ⁵⁴, T. Ackernley ⁵⁸,
 B. Adeva ⁴⁴, M. Adinolfi ⁵², P. Adlarson ⁷⁸, C. Agapopoulou ⁴⁶, C.A. Aidala ⁷⁹, Z. Ajaltouni¹¹,
 S. Akar ⁶³, K. Akiba ³⁵, P. Albicocco ²⁵, J. Albrecht ¹⁷, F. Alessio ⁴⁶, M. Alexander ⁵⁷,
 A. Alfonso Albero ⁴³, Z. Aliouche ⁶⁰, P. Alvarez Cartelle ⁵³, R. Amalric ¹⁵, S. Amato ³,
 J.L. Amey ⁵², Y. Amhis ^{13,46}, L. An ⁶, L. Anderlini ²⁴, M. Andersson ⁴⁸, A. Andreianov ⁴¹,
 P. Andreola ⁴⁸, M. Andreotti ²³, D. Andreou ⁶⁶, A. Anelli ^{28,o}, D. Ao ⁷, F. Archilli ^{34,u},
 M. Argenton ²³, S. Arguedas Cuendis ⁹, A. Artamonov ⁴¹, M. Artuso ⁶⁶, E. Aslanides ¹²,
 M. Atzeni ⁶², B. Audurier ¹⁴, D. Bacher ⁶¹, I. Bachiller Perea ¹⁰, S. Bachmann ¹⁹,
 M. Bachmayer ⁴⁷, J.J. Back ⁵⁴, P. Baladron Rodriguez ⁴⁴, V. Balagura ¹⁴, W. Baldini ²³,
 J. Baptista de Souza Leite ², M. Barbetti ^{24,l}, I.R. Barbosa ⁶⁷, R.J. Barlow ⁶⁰, S. Barsuk ¹³,
 W. Barter ⁵⁶, M. Bartolini ⁵³, J. Bartz ⁶⁶, F. Baryshnikov ⁴¹, J.M. Basels ¹⁶, G. Bassi ^{32,r},
 B. Batsukh ⁵, A. Battig ¹⁷, A. Bay ⁴⁷, A. Beck ⁵⁴, M. Becker ¹⁷, F. Bedeschi ³²,
 I.B. Bediaga ², A. Beiter ⁶⁶, S. Belin ⁴⁴, V. Bellee ⁴⁸, K. Belous ⁴¹, I. Belov ²⁶, I. Belyaev ⁴¹,
 G. Benane ¹², G. Bencivenni ²⁵, E. Ben-Haim ¹⁵, A. Berezhnoy ⁴¹, R. Bernet ⁴⁸,
 S. Bernet Andres ⁴², H.C. Bernstein ⁶⁶, C. Bertella ⁶⁰, A. Bertolin ³⁰, C. Betancourt ⁴⁸,
 F. Betti ⁵⁶, J. Bex ⁵³, Ia. Bezshyiko ⁴⁸, J. Bhom ³⁸, M.S. Bieker ¹⁷, N.V. Biesuz ²³,
 P. Billoir ¹⁵, A. Biolchini ³⁵, M. Birch ⁵⁹, F.C.R. Bishop ¹⁰, A. Bitadze ⁶⁰, A. Bizzeti ¹,
 M.P. Blago ⁵³, T. Blake ⁵⁴, F. Blanc ⁴⁷, J.E. Blank ¹⁷, S. Blusk ⁶⁶, D. Bobulska ⁵⁷,
 V. Bocharnikov ⁴¹, J.A. Boelhauve ¹⁷, O. Boente Garcia ¹⁴, T. Boettcher ⁶³, A. Bohare ⁵⁶,
 A. Boldyrev ⁴¹, C.S. Bolognani ⁷⁶, R. Bolzonella ^{23,k}, N. Bondar ⁴¹, F. Borgato ^{30,46},
 S. Borghi ⁶⁰, M. Borsato ^{28,o}, J.T. Borsuk ³⁸, S.A. Bouchiba ⁴⁷, T.J.V. Bowcock ⁵⁸,
 A. Boyer ⁴⁶, C. Bozzi ²³, M.J. Bradley ⁵⁹, S. Braun ⁶⁴, A. Brea Rodriguez ⁴⁴, N. Breer ¹⁷,
 J. Brodzicka ³⁸, A. Brossa Gonzalo ⁴⁴, J. Brown ⁵⁸, D. Brundu ²⁹, A. Buonaura ⁴⁸,
 L. Buonincontri ³⁰, A.T. Burke ⁶⁰, C. Burr ⁴⁶, A. Bursche ⁶⁹, A. Butkevich ⁴¹, J.S. Butter ⁵³,
 J. Buytaert ⁴⁶, W. Byczynski ⁴⁶, S. Cadeddu ²⁹, H. Cai ⁷¹, R. Calabrese ^{23,k}, L. Calefice ¹⁷,
 S. Cali ²⁵, M. Calvi ^{28,o}, M. Calvo Gomez ⁴², J. Cambon Bouzas ⁴⁴, P. Campana ²⁵,
 D.H. Campora Perez ⁷⁶, A.F. Campoverde Quezada ⁷, S. Capelli ^{28,o}, L. Capriotti ²³,
 R. Caravaca-Mora ⁹, A. Carbone ^{22,i}, L. Carcedo Salgado ⁴⁴, R. Cardinale ^{26,m}, A. Cardini ²⁹,
 P. Carniti ^{28,o}, L. Carus ¹⁹, A. Casais Vidal ⁶², R. Caspary ¹⁹, G. Casse ⁵⁸,
 J. Castro Godinez ⁹, M. Cattaneo ⁴⁶, G. Cavallero ²³, V. Cavallini ^{23,k}, S. Celani ⁴⁷,
 J. Cerasoli ¹², D. Cervenkov ⁶¹, S. Cesare ^{27,n}, A.J. Chadwick ⁵⁸, I. Chahrour ⁷⁹,
 M. Charles ¹⁵, Ph. Charpentier ⁴⁶, C.A. Chavez Barajas ⁵⁸, M. Chefdeville ¹⁰, C. Chen ¹²,
 S. Chen ⁵, Z. Chen ⁷, A. Chernov ³⁸, S. Chernyshenko ⁵⁰, V. Chobanova ^{44,y}, S. Cholak ⁴⁷,
 M. Chrzaszcz ³⁸, A. Chubykin ⁴¹, V. Chulikov ⁴¹, P. Ciambrone ²⁵, M.F. Cicala ⁵⁴,
 X. Cid Vidal ⁴⁴, G. Ciezarek ⁴⁶, P. Cifra ⁴⁶, P.E.L. Clarke ⁵⁶, M. Clemencic ⁴⁶, H.V. Cliff ⁵³,
 J. Closier ⁴⁶, J.L. Cobbledick ⁶⁰, C. Cocha Toapaxi ¹⁹, V. Coco ⁴⁶, J. Cogan ¹²,
 E. Cogneras ¹¹, L. Cojocariu ⁴⁰, P. Collins ⁴⁶, T. Colombo ⁴⁶, A. Comerma-Montells ⁴³,
 L. Congedo ²¹, A. Contu ²⁹, N. Cooke ⁵⁷, I. Corredoira ⁴⁴, A. Correia ¹⁵, G. Corti ⁴⁶,
 J.J. Cottee Meldrum ⁵², B. Couturier ⁴⁶, D.C. Craik ⁴⁸, M. Cruz Torres ^{2,g}, E. Curras Rivera ⁴⁷,
 R. Currie ⁵⁶, C.L. Da Silva ⁶⁵, S. Dadabaev ⁴¹, L. Dai ⁶⁸, X. Dai ⁶, E. Dall'Occo ¹⁷,
 J. Dalseno ⁴⁴, C. D'Ambrosio ⁴⁶, J. Daniel ¹¹, A. Danilina ⁴¹, P. d'Argent ²¹, A. Davidson ⁵⁴,
 J.E. Davies ⁶⁰, A. Davis ⁶⁰, O. De Aguiar Francisco ⁶⁰, C. De Angelis ^{29,j}, J. de Boer ³⁵,

- K. De Bruyn $\textcolor{blue}{ID}^{75}$, S. De Capua $\textcolor{blue}{ID}^{60}$, M. De Cian $\textcolor{blue}{ID}^{19,46}$, U. De Freitas Carneiro Da Graca $\textcolor{blue}{ID}^{2,b}$, E. De Lucia $\textcolor{blue}{ID}^{25}$, J.M. De Miranda $\textcolor{blue}{ID}^2$, L. De Paula $\textcolor{blue}{ID}^3$, M. De Serio $\textcolor{blue}{ID}^{21,h}$, D. De Simone $\textcolor{blue}{ID}^{48}$, P. De Simone $\textcolor{blue}{ID}^{25}$, F. De Vellis $\textcolor{blue}{ID}^{17}$, J.A. de Vries $\textcolor{blue}{ID}^{76}$, F. Debernardis $\textcolor{blue}{ID}^{21,h}$, D. Decamp $\textcolor{blue}{ID}^{10}$, V. Dedu $\textcolor{blue}{ID}^{12}$, L. Del Buono $\textcolor{blue}{ID}^{15}$, B. Delaney $\textcolor{blue}{ID}^{62}$, H.-P. Dembinski $\textcolor{blue}{ID}^{17}$, J. Deng $\textcolor{blue}{ID}^8$, V. Denysenko $\textcolor{blue}{ID}^{48}$, O. Deschamps $\textcolor{blue}{ID}^{11}$, F. Dettori $\textcolor{blue}{ID}^{29,j}$, B. Dey $\textcolor{blue}{ID}^{74}$, P. Di Nezza $\textcolor{blue}{ID}^{25}$, I. Diachkov $\textcolor{blue}{ID}^{41}$, S. Didenko $\textcolor{blue}{ID}^{41}$, S. Ding $\textcolor{blue}{ID}^{66}$, V. Dobishuk $\textcolor{blue}{ID}^{50}$, A.D. Docheva $\textcolor{blue}{ID}^{57}$, A. Dolmatov $\textcolor{blue}{ID}^{41}$, C. Dong $\textcolor{blue}{ID}^4$, A.M. Donohoe $\textcolor{blue}{ID}^{20}$, F. Dordei $\textcolor{blue}{ID}^{29}$, A.C. dos Reis $\textcolor{blue}{ID}^2$, L. Douglas $\textcolor{blue}{ID}^{57}$, A.G. Downes $\textcolor{blue}{ID}^{10}$, W. Duan $\textcolor{blue}{ID}^{69}$, P. Duda $\textcolor{blue}{ID}^{77}$, M.W. Dudek $\textcolor{blue}{ID}^{38}$, L. Dufour $\textcolor{blue}{ID}^{46}$, V. Duk $\textcolor{blue}{ID}^{31}$, P. Durante $\textcolor{blue}{ID}^{46}$, M.M. Duras $\textcolor{blue}{ID}^{77}$, J.M. Durham $\textcolor{blue}{ID}^{65}$, A. Dziurda $\textcolor{blue}{ID}^{38}$, A. Dzyuba $\textcolor{blue}{ID}^{41}$, S. Easo $\textcolor{blue}{ID}^{55,46}$, E. Eckstein $\textcolor{blue}{ID}^{73}$, U. Egede $\textcolor{blue}{ID}^1$, A. Egorychev $\textcolor{blue}{ID}^{41}$, V. Egorychev $\textcolor{blue}{ID}^{41}$, C. Eirea Orro $\textcolor{blue}{ID}^{44}$, S. Eisenhardt $\textcolor{blue}{ID}^{56}$, E. Ejopu $\textcolor{blue}{ID}^{60}$, S. Ek-In $\textcolor{blue}{ID}^{47}$, L. Eklund $\textcolor{blue}{ID}^{78}$, M. Elashri $\textcolor{blue}{ID}^{63}$, J. Ellbracht $\textcolor{blue}{ID}^{17}$, S. Ely $\textcolor{blue}{ID}^{59}$, A. Ene $\textcolor{blue}{ID}^{40}$, E. Epple $\textcolor{blue}{ID}^{63}$, S. Escher $\textcolor{blue}{ID}^{16}$, J. Eschle $\textcolor{blue}{ID}^{48}$, S. Esen $\textcolor{blue}{ID}^{48}$, T. Evans $\textcolor{blue}{ID}^{60}$, F. Fabiano $\textcolor{blue}{ID}^{29,j,46}$, L.N. Falcao $\textcolor{blue}{ID}^2$, Y. Fan $\textcolor{blue}{ID}^7$, B. Fang $\textcolor{blue}{ID}^{71,13}$, L. Fantini $\textcolor{blue}{ID}^{31,q}$, M. Faria $\textcolor{blue}{ID}^{47}$, K. Farmer $\textcolor{blue}{ID}^{56}$, D. Fazzini $\textcolor{blue}{ID}^{28,o}$, L. Felkowski $\textcolor{blue}{ID}^{77}$, M. Feng $\textcolor{blue}{ID}^{5,7}$, M. Feo $\textcolor{blue}{ID}^{46}$, M. Fernandez Gomez $\textcolor{blue}{ID}^{44}$, A.D. Fernez $\textcolor{blue}{ID}^{64}$, F. Ferrari $\textcolor{blue}{ID}^{22}$, F. Ferreira Rodrigues $\textcolor{blue}{ID}^3$, S. Ferreres Sole $\textcolor{blue}{ID}^{35}$, M. Ferrillo $\textcolor{blue}{ID}^{48}$, M. Ferro-Luzzi $\textcolor{blue}{ID}^{46}$, S. Filippov $\textcolor{blue}{ID}^{41}$, R.A. Fini $\textcolor{blue}{ID}^{21}$, M. Fiorini $\textcolor{blue}{ID}^{23,k}$, M. Firlej $\textcolor{blue}{ID}^{37}$, K.M. Fischer $\textcolor{blue}{ID}^{61}$, D.S. Fitzgerald $\textcolor{blue}{ID}^{79}$, C. Fitzpatrick $\textcolor{blue}{ID}^{60}$, T. Fiutowski $\textcolor{blue}{ID}^{37}$, F. Fleuret $\textcolor{blue}{ID}^{14}$, M. Fontana $\textcolor{blue}{ID}^{22}$, F. Fontanelli $\textcolor{blue}{ID}^{26,m}$, L.F. Foreman $\textcolor{blue}{ID}^{60}$, R. Forty $\textcolor{blue}{ID}^{46}$, D. Foulds-Holt $\textcolor{blue}{ID}^{53}$, M. Franco Sevilla $\textcolor{blue}{ID}^{64}$, M. Frank $\textcolor{blue}{ID}^{46}$, E. Franzoso $\textcolor{blue}{ID}^{23,k}$, G. Frau $\textcolor{blue}{ID}^{19}$, C. Frei $\textcolor{blue}{ID}^{46}$, D.A. Friday $\textcolor{blue}{ID}^{60}$, L. Frontini $\textcolor{blue}{ID}^{27,n}$, J. Fu $\textcolor{blue}{ID}^7$, Q. Fuehring $\textcolor{blue}{ID}^{17}$, Y. Fujii $\textcolor{blue}{ID}^1$, T. Fulghesu $\textcolor{blue}{ID}^{15}$, E. Gabriel $\textcolor{blue}{ID}^{35}$, G. Galati $\textcolor{blue}{ID}^{21,h}$, M.D. Galati $\textcolor{blue}{ID}^{35}$, A. Gallas Torreira $\textcolor{blue}{ID}^{44}$, D. Galli $\textcolor{blue}{ID}^{22,i}$, S. Gambetta $\textcolor{blue}{ID}^{56}$, M. Gandelman $\textcolor{blue}{ID}^3$, P. Gandini $\textcolor{blue}{ID}^{27}$, H. Gao $\textcolor{blue}{ID}^7$, R. Gao $\textcolor{blue}{ID}^{61}$, Y. Gao $\textcolor{blue}{ID}^8$, Y. Gao $\textcolor{blue}{ID}^6$, Y. Gao $\textcolor{blue}{ID}^8$, M. Garau $\textcolor{blue}{ID}^{29,j}$, L.M. Garcia Martin $\textcolor{blue}{ID}^{47}$, P. Garcia Moreno $\textcolor{blue}{ID}^{43}$, J. García Pardiñas $\textcolor{blue}{ID}^{46}$, B. Garcia Plana $\textcolor{blue}{ID}^{44}$, K.G. Garg $\textcolor{blue}{ID}^8$, L. Garrido $\textcolor{blue}{ID}^{43}$, C. Gaspar $\textcolor{blue}{ID}^{46}$, R.E. Geertsema $\textcolor{blue}{ID}^{35}$, L.L. Gerken $\textcolor{blue}{ID}^{17}$, E. Gersabeck $\textcolor{blue}{ID}^{60}$, M. Gersabeck $\textcolor{blue}{ID}^{60}$, T. Gershon $\textcolor{blue}{ID}^{54}$, Z. Ghorbanimoghaddam $\textcolor{blue}{ID}^{52}$, L. Giambastiani $\textcolor{blue}{ID}^{30}$, F.I. Giasemis $\textcolor{blue}{ID}^{15,e}$, V. Gibson $\textcolor{blue}{ID}^{53}$, H.K. Giemza $\textcolor{blue}{ID}^{39}$, A.L. Gilman $\textcolor{blue}{ID}^{61}$, M. Giovannetti $\textcolor{blue}{ID}^{25}$, A. Gioventù $\textcolor{blue}{ID}^{43}$, P. Gironella Gironell $\textcolor{blue}{ID}^{43}$, C. Giugliano $\textcolor{blue}{ID}^{23,k}$, M.A. Giza $\textcolor{blue}{ID}^{38}$, E.L. Gkougkousis $\textcolor{blue}{ID}^{59}$, F.C. Glaser $\textcolor{blue}{ID}^{13,19}$, V.V. Gligorov $\textcolor{blue}{ID}^{15}$, C. Göbel $\textcolor{blue}{ID}^{67}$, E. Golobardes $\textcolor{blue}{ID}^{42}$, D. Golubkov $\textcolor{blue}{ID}^{41}$, A. Golutvin $\textcolor{blue}{ID}^{59,41,46}$, A. Gomes $\textcolor{blue}{ID}^{2,a,\dagger}$, S. Gomez Fernandez $\textcolor{blue}{ID}^{43}$, F. Goncalves Abrantes $\textcolor{blue}{ID}^{61}$, M. Goncerz $\textcolor{blue}{ID}^{38}$, G. Gong $\textcolor{blue}{ID}^4$, J.A. Gooding $\textcolor{blue}{ID}^{17}$, I.V. Gorelov $\textcolor{blue}{ID}^{41}$, C. Gotti $\textcolor{blue}{ID}^{28}$, J.P. Grabowski $\textcolor{blue}{ID}^{73}$, L.A. Granado Cardoso $\textcolor{blue}{ID}^{46}$, E. Graugés $\textcolor{blue}{ID}^{43}$, E. Graverini $\textcolor{blue}{ID}^{47,s}$, L. Grazette $\textcolor{blue}{ID}^{54}$, G. Graziani $\textcolor{blue}{ID}$, A.T. Grecu $\textcolor{blue}{ID}^{40}$, L.M. Greeven $\textcolor{blue}{ID}^{35}$, N.A. Grieser $\textcolor{blue}{ID}^{63}$, L. Grillo $\textcolor{blue}{ID}^{57}$, S. Gromov $\textcolor{blue}{ID}^{41}$, C. Gu $\textcolor{blue}{ID}^{14}$, M. Guarise $\textcolor{blue}{ID}^{23}$, M. Guittiere $\textcolor{blue}{ID}^{13}$, V. Guliaeva $\textcolor{blue}{ID}^{41}$, P.A. Günther $\textcolor{blue}{ID}^{19}$, A.-K. Guseinov $\textcolor{blue}{ID}^{41}$, E. Gushchin $\textcolor{blue}{ID}^{41}$, Y. Guz $\textcolor{blue}{ID}^{6,41,46}$, T. Gys $\textcolor{blue}{ID}^{46}$, T. Hadavizadeh $\textcolor{blue}{ID}^1$, C. Hadjivasilou $\textcolor{blue}{ID}^{64}$, G. Haefeli $\textcolor{blue}{ID}^{47}$, C. Haen $\textcolor{blue}{ID}^{46}$, J. Haimberger $\textcolor{blue}{ID}^{46}$, M. Hajheidari $\textcolor{blue}{ID}^{46}$, T. Halewood-leagas $\textcolor{blue}{ID}^{58}$, M.M. Halvorsen $\textcolor{blue}{ID}^{46}$, P.M. Hamilton $\textcolor{blue}{ID}^{64}$, J. Hammerich $\textcolor{blue}{ID}^{58}$, Q. Han $\textcolor{blue}{ID}^8$, X. Han $\textcolor{blue}{ID}^{19}$, S. Hansmann-Menzemer $\textcolor{blue}{ID}^{19}$, L. Hao $\textcolor{blue}{ID}^7$, N. Harnew $\textcolor{blue}{ID}^{61}$, T. Harrison $\textcolor{blue}{ID}^{58}$, M. Hartmann $\textcolor{blue}{ID}^{13}$, C. Hasse $\textcolor{blue}{ID}^{46}$, J. He $\textcolor{blue}{ID}^{7,c}$, K. Heijhoff $\textcolor{blue}{ID}^{35}$, F. Hemmer $\textcolor{blue}{ID}^{46}$, C. Henderson $\textcolor{blue}{ID}^{63}$, R.D.L. Henderson $\textcolor{blue}{ID}^{1,54}$, A.M. Hennequin $\textcolor{blue}{ID}^{46}$, K. Hennessy $\textcolor{blue}{ID}^{58}$, L. Henry $\textcolor{blue}{ID}^{47}$, J. Herd $\textcolor{blue}{ID}^{59}$, P. Herrero Gascon $\textcolor{blue}{ID}^{19}$, J. Heuel $\textcolor{blue}{ID}^{16}$, A. Hicheur $\textcolor{blue}{ID}^3$, G. Hijano Mendizabal $\textcolor{blue}{ID}^{48}$, D. Hill $\textcolor{blue}{ID}^{47}$, S.E. Hollitt $\textcolor{blue}{ID}^{17}$, J. Horswill $\textcolor{blue}{ID}^{60}$, R. Hou $\textcolor{blue}{ID}^8$, Y. Hou $\textcolor{blue}{ID}^{10}$, N. Howarth $\textcolor{blue}{ID}^{58}$, J. Hu $\textcolor{blue}{ID}^{19}$, J. Hu $\textcolor{blue}{ID}^{69}$, W. Hu $\textcolor{blue}{ID}^6$, X. Hu $\textcolor{blue}{ID}^4$, W. Huang $\textcolor{blue}{ID}^7$, W. Hulsbergen $\textcolor{blue}{ID}^{35}$, R.J. Hunter $\textcolor{blue}{ID}^{54}$, M. Hushchyn $\textcolor{blue}{ID}^{41}$, D. Hutchcroft $\textcolor{blue}{ID}^{58}$, M. Idzik $\textcolor{blue}{ID}^{37}$, D. Ilin $\textcolor{blue}{ID}^{41}$, P. Ilten $\textcolor{blue}{ID}^{63}$, A. Inglessi $\textcolor{blue}{ID}^{41}$, A. Iniukhin $\textcolor{blue}{ID}^{41}$, A. Ishteev $\textcolor{blue}{ID}^{41}$, K. Ivshin $\textcolor{blue}{ID}^{41}$, R. Jacobsson $\textcolor{blue}{ID}^{46}$, H. Jage $\textcolor{blue}{ID}^{16}$,

- S.J. Jaimes Elles^{ID}^{45,72}, S. Jakobsen^{ID}⁴⁶, E. Jans^{ID}³⁵, B.K. Jashal^{ID}⁴⁵, A. Jawahery^{ID}^{64,46}, V. Jevtic^{ID}¹⁷, E. Jiang^{ID}⁶⁴, X. Jiang^{ID}^{5,7}, Y. Jiang^{ID}⁷, Y.J. Jiang^{ID}⁶, M. John^{ID}⁶¹, D. Johnson^{ID}⁵¹, C.R. Jones^{ID}⁵³, T.P. Jones^{ID}⁵⁴, S. Joshi^{ID}³⁹, B. Jost^{ID}⁴⁶, N. Jurik^{ID}⁴⁶, I. Juszczak^{ID}³⁸, D. Kaminaris^{ID}⁴⁷, S. Kandybei^{ID}⁴⁹, Y. Kang^{ID}⁴, M. Karacson^{ID}⁴⁶, D. Karpenkov^{ID}⁴¹, M. Karpov^{ID}⁴¹, A.M. Kauniskangas^{ID}⁴⁷, J.W. Kautz^{ID}⁶³, F. Keizer^{ID}⁴⁶, D.M. Keller^{ID}⁶⁶, M. Kenzie^{ID}⁵³, T. Ketel^{ID}³⁵, B. Khanji^{ID}⁶⁶, A. Kharisova^{ID}⁴¹, S. Kholodenko^{ID}³², G. Khreich^{ID}¹³, T. Kirn^{ID}¹⁶, V.S. Kirsebom^{ID}⁴⁷, O. Kitouni^{ID}⁶², S. Klaver^{ID}³⁶, N. Kleijne^{ID}^{32,r}, K. Klimaszewski^{ID}³⁰, M.R. Kmiec^{ID}³⁹, S. Koliiev^{ID}⁵⁰, L. Kolk^{ID}¹⁷, A. Konoplyannikov^{ID}⁴¹, P. Kopciewicz^{ID}^{37,46}, P. Koppenburg^{ID}³⁵, M. Korolev^{ID}⁴¹, I. Kostiuk^{ID}³⁵, O. Kot⁵⁰, S. Kotriakhova^{ID}, A. Kozachuk^{ID}⁴¹, P. Kravchenko^{ID}⁴¹, L. Kravchuk^{ID}⁴¹, M. Kreps^{ID}⁵⁴, S. Kretzschmar^{ID}¹⁶, P. Krokovny^{ID}⁴¹, W. Krupa^{ID}⁶⁶, W. Krzemien^{ID}³⁹, J. Kubat¹⁹, S. Kubis^{ID}⁷⁷, W. Kucewicz^{ID}³⁸, M. Kucharczyk^{ID}³⁸, V. Kudryavtsev^{ID}⁴¹, E. Kulikova^{ID}⁴¹, A. Kupsc^{ID}⁷⁸, B.K. Kutsenko^{ID}¹², D. Lacarrere^{ID}⁴⁶, A. Lai^{ID}²⁹, A. Lampis^{ID}²⁹, D. Lancierini^{ID}⁴⁸, C. Landesa Gomez^{ID}⁴⁴, J.J. Lane^{ID}¹, R. Lane^{ID}⁵², C. Langenbruch^{ID}¹⁹, J. Langer^{ID}¹⁷, O. Lantwin^{ID}⁴¹, T. Latham^{ID}⁵⁴, F. Lazzari^{ID}^{32,s}, C. Lazzeroni^{ID}⁵¹, R. Le Gac^{ID}¹², S.H. Lee^{ID}⁷⁹, R. Lefèvre^{ID}¹¹, A. Leflat^{ID}⁴¹, S. Legotin^{ID}⁴¹, M. Lehuraux^{ID}⁵⁴, O. Leroy^{ID}¹², T. Lesiak^{ID}³⁸, B. Leverington^{ID}¹⁹, A. Li^{ID}⁴, H. Li^{ID}⁶⁹, K. Li^{ID}⁸, L. Li^{ID}⁶⁰, P. Li^{ID}⁴⁶, P.-R. Li^{ID}⁷⁰, S. Li^{ID}⁸, T. Li^{ID}^{5,d}, T. Li^{ID}⁶⁹, Y. Li^{ID}⁸, Y. Li^{ID}⁵, Z. Li^{ID}⁶⁶, Z. Lian^{ID}⁴, X. Liang^{ID}⁶⁶, C. Lin^{ID}⁷, T. Lin^{ID}⁵⁵, R. Lindner^{ID}⁴⁶, V. Lisovskyi^{ID}⁴⁷, R. Litvinov^{ID}^{29,j}, F.L. Liu^{ID}¹, G. Liu^{ID}⁶⁹, H. Liu^{ID}⁷, K. Liu^{ID}⁷⁰, Q. Liu^{ID}⁷, S. Liu^{ID}^{5,7}, Y. Liu^{ID}⁵⁶, Y. Liu^{ID}⁷⁰, Y.L. Liu^{ID}⁵⁹, A. Lobo Salvia^{ID}⁴³, A. Loi^{ID}²⁹, J. Lomba Castro^{ID}⁴⁴, T. Long^{ID}⁵³, J.H. Lopes^{ID}³, A. Lopez Huertas^{ID}⁴³, S. López Soliño^{ID}⁴⁴, G.H. Lovell^{ID}⁵³, C. Lucarelli^{ID}^{24,l}, D. Lucchesi^{ID}^{30,p}, S. Luchuk^{ID}⁴¹, M. Lucio Martinez^{ID}⁷⁶, V. Lukashenko^{ID}^{35,50}, Y. Luo^{ID}⁶, A. Lupato^{ID}³⁰, E. Luppi^{ID}^{23,k}, K. Lynch^{ID}²⁰, X.-R. Lyu^{ID}⁷, G.M. Ma^{ID}⁴, R. Ma^{ID}⁷, S. Maccolini^{ID}¹⁷, F. Machefert^{ID}¹³, F. Maciuc^{ID}⁴⁰, B.M. Mack^{ID}⁶⁶, I. Mackay^{ID}⁶¹, L.M. Mackey^{ID}⁶⁶, L.R. Madhan Mohan^{ID}⁵³, M.M. Madurai^{ID}⁵¹, A. Maevskiy^{ID}⁴¹, D. Magdalinski^{ID}³⁵, D. Maisuzenko^{ID}⁴¹, M.W. Majewski³⁷, J.J. Malczewski^{ID}³⁸, S. Malde^{ID}⁶¹, B. Malecki^{ID}^{38,46}, L. Malentacca^{ID}⁴⁶, A. Malinin^{ID}⁴¹, T. Maltsev^{ID}⁴¹, G. Manca^{ID}^{29,j}, G. Mancinelli^{ID}¹², C. Mancuso^{ID}^{27,13,n}, R. Manera Escalero⁴³, D. Manuzzi^{ID}²², D. Marangotto^{ID}^{27,n}, J.F. Marchand^{ID}¹⁰, R. Marchevski^{ID}⁴⁷, U. Marconi^{ID}²², S. Mariani^{ID}⁴⁶, C. Marin Benito^{ID}⁴³, J. Marks^{ID}¹⁹, A.M. Marshall^{ID}⁵², P.J. Marshall⁵⁸, G. Martelli^{ID}^{31,q}, G. Martellotti^{ID}³³, L. Martinazzoli^{ID}⁴⁶, M. Martinelli^{ID}^{28,o}, D. Martinez Santos^{ID}⁴⁴, F. Martinez Vidal^{ID}⁴⁵, A. Massafferri^{ID}², M. Materok^{ID}¹⁶, R. Matev^{ID}⁴⁶, A. Mathad^{ID}⁴⁸, V. Matiunin^{ID}⁴¹, C. Matteuzzi^{ID}⁶⁶, K.R. Mattioli^{ID}¹⁴, A. Mauri^{ID}⁵⁹, E. Maurice^{ID}¹⁴, J. Mauricio^{ID}⁴³, P. Mayencourt^{ID}⁴⁷, M. Mazurek^{ID}⁴⁶, M. McCann^{ID}⁵⁹, L. Mcconnell^{ID}²⁰, T.H. McGrath^{ID}⁶⁰, N.T. McHugh^{ID}⁵⁷, A. McNab^{ID}⁶⁰, R. McNulty^{ID}²⁰, B. Meadows^{ID}⁶³, G. Meier^{ID}¹⁷, D. Melnychuk^{ID}³⁹, M. Merk^{ID}^{35,76}, A. Merli^{ID}^{27,n}, L. Meyer Garcia^{ID}³, D. Miao^{ID}^{5,7}, H. Miao^{ID}⁷, M. Mikhasenko^{ID}^{73,f}, D.A. Milanes^{ID}⁷², A. Minotti^{ID}^{28,o}, E. Minuccia^{ID}⁶⁶, T. Miralles^{ID}¹¹, S.E. Mitchell^{ID}⁵⁶, B. Mitreska^{ID}¹⁷, D.S. Mitzel^{ID}¹⁷, A. Modak^{ID}⁵⁵, A. Mödden^{ID}¹⁷, R.A. Mohammed^{ID}⁶¹, R.D. Moise^{ID}¹⁶, S. Mokhnenco^{ID}⁴¹, T. Mombächer^{ID}⁴⁶, M. Monk^{ID}^{54,1}, I.A. Monroy^{ID}⁷², S. Monteil^{ID}¹¹, A. Morcillo Gomez^{ID}⁴⁴, G. Morello^{ID}²⁵, M.J. Morello^{ID}^{32,r}, M.P. Morgenthaler^{ID}¹⁹, J. Moron^{ID}³⁷, A.B. Morris^{ID}⁴⁶, A.G. Morris^{ID}¹², R. Mountain^{ID}⁶⁶, H. Mu^{ID}⁴, Z.M. Mu^{ID}⁶, E. Muhammad^{ID}⁵⁴, F. Muheim^{ID}⁵⁶, M. Mulder^{ID}⁷⁵, K. Müller^{ID}⁴⁸, F. Múnoz-Rojas^{ID}⁹, R. Murta^{ID}⁵⁹, P. Naik^{ID}⁵⁸, T. Nakada^{ID}⁴⁷, R. Nandakumar^{ID}⁵⁵, T. Nanut^{ID}⁴⁶,

- I. Nasteva ID^3 , M. Needham ID^{56} , N. Neri $\text{ID}^{27,n}$, S. Neubert ID^{73} , N. Neufeld ID^{46} , P. Neustroev ID^{41} , R. Newcombe ID^{59} , J. Nicolini $\text{ID}^{17,13}$, D. Nicotra ID^{76} , E.M. Niel ID^{47} , N. Nikitin ID^{41} , P. Nogga ID^{73} , N.S. Nolte ID^{62} , C. Normand $\text{ID}^{10,29}$, J. Novoa Fernandez ID^{44} , G. Nowak ID^{63} , C. Nunez ID^{79} , H.N. Nur ID^{57} , A. Oblakowska-Mucha ID^{37} , V. Obraztsov ID^{41} , T. Oeser ID^{16} , S. Okamura $\text{ID}^{23,k,46}$, R. Oldeman $\text{ID}^{29,j}$, F. Oliva ID^{56} , M. Olocco ID^{17} , C.J.G. Onderwater ID^{76} , R.H. O'Neil ID^{56} , J.M. Otalora Goicochea ID^3 , T. Ovsiannikova ID^{41} , P. Owen ID^{48} , A. Oyanguren ID^{45} , O. Ozcelik ID^{56} , K.O. Padeken ID^{73} , B. Pagare ID^{54} , P.R. Pais ID^{19} , T. Pajero ID^{61} , A. Palano ID^{21} , M. Palutan ID^{25} , G. Panshin ID^{41} , L. Paolucci ID^{54} , A. Papanestis ID^{55} , M. Pappagallo $\text{ID}^{21,h}$, L.L. Pappalardo $\text{ID}^{23,k}$, C. Pappenheimer ID^{63} , C. Parkes ID^{60} , B. Passalacqua $\text{ID}^{23,k}$, G. Passaleva ID^{24} , D. Passaro $\text{ID}^{32,r}$, A. Pastore ID^{21} , M. Patel ID^{59} , J. Patoc ID^{61} , C. Patrignani $\text{ID}^{22,i}$, C.J. Pawley ID^{76} , A. Pellegrino ID^{35} , M. Pepe Altarelli ID^{25} , S. Perazzini ID^{22} , D. Pereima ID^{41} , A. Pereiro Castro ID^{44} , P. Perret ID^{11} , A. Perro ID^{46} , K. Petridis ID^{52} , A. Petrolini $\text{ID}^{26,m}$, S. Petrucci ID^{56} , J.P. Pfaller ID^{63} , H. Pham ID^{66} , L. Pica $\text{ID}^{32,r}$, M. Piccini ID^{31} , B. Pietrzyk ID^{10} , G. Pietrzyk ID^{13} , D. Pinci ID^{33} , F. Pisani ID^{46} , M. Pizzichemi $\text{ID}^{28,o}$, V. Placinta ID^{40} , M. Plo Casasus ID^{44} , F. Polci $\text{ID}^{15,46}$, M. Poli Lener ID^{25} , A. Poluektov ID^{12} , N. Polukhina ID^{41} , I. Polyakov ID^{46} , E. Polycarpo ID^3 , S. Ponce ID^{46} , D. Popov ID^7 , S. Poslavskii ID^{41} , K. Prasanth ID^{38} , C. Prouve ID^{44} , V. Pugatch ID^{50} , G. Punzi $\text{ID}^{32,s}$, W. Qian ID^7 , N. Qin ID^4 , S. Qu ID^4 , R. Quagliani ID^{47} , R.I. Rabadan Trejo ID^{54} , B. Rachwal ID^{37} , J.H. Rademacker ID^{52} , M. Rama ID^{32} , M. Ramírez García ID^{79} , M. Ramos Pernas ID^{54} , M.S. Rangel ID^3 , F. Ratnikov ID^{41} , G. Raven ID^{36} , M. Rebollo De Miguel ID^{45} , F. Redi ID^{46} , J. Reich ID^{52} , F. Reiss ID^{60} , Z. Ren ID^7 , P.K. Resmi ID^{61} , R. Ribatti $\text{ID}^{32,r}$, G.R. Ricart $\text{ID}^{14,80}$, D. Riccardi $\text{ID}^{32,r}$, S. Ricciardi ID^{55} , K. Richardson ID^{62} , M. Richardson-Slipper ID^{56} , K. Rinnert ID^{58} , P. Robbe ID^{13} , G. Robertson ID^{57} , E. Rodrigues $\text{ID}^{58,46}$, E. Rodriguez Fernandez ID^{44} , J.A. Rodriguez Lopez ID^{72} , E. Rodriguez Rodriguez ID^{44} , A. Rogovskiy ID^{55} , D.L. Rolf ID^{46} , A. Rollings ID^{61} , P. Roloff ID^{46} , V. Romanovskiy ID^{41} , M. Romero Lamas ID^{44} , A. Romero Vidal ID^{44} , G. Romolini ID^{23} , F. Ronchetti ID^{47} , M. Rotondo ID^{25} , S.R. Roy ID^{19} , M.S. Rudolph ID^{66} , T. Ruf ID^{46} , M. Ruiz Diaz ID^{19} , R.A. Ruiz Fernandez ID^{44} , J. Ruiz Vidal $\text{ID}^{78,z}$, A. Ryzhikov ID^{41} , J. Ryzka ID^{37} , J.J. Saborido Silva ID^{44} , R. Sadek ID^{14} , N. Sagidova ID^{41} , N. Sahoo ID^{51} , B. Saitta $\text{ID}^{29,j}$, M. Salomon $\text{ID}^{28,o}$, C. Sanchez Gras ID^{35} , I. Sanderswood ID^{45} , R. Santacesaria ID^{33} , C. Santamarina Rios ID^{44} , M. Santimaria ID^{25} , L. Santoro ID^2 , E. Santovetti ID^{34} , A. Saputri $\text{ID}^{23,46}$, D. Saranin ID^{41} , G. Sarpis ID^{56} , M. Sarpis ID^{73} , A. Sarti ID^{33} , C. Satriano $\text{ID}^{33,t}$, A. Satta ID^{34} , M. Saur ID^6 , D. Savrina ID^{41} , H. Sazak ID^{11} , L.G. Scantlebury Smead ID^{61} , A. Scarabotto ID^{15} , S. Schael ID^{16} , S. Scherl ID^{58} , A.M. Schertz ID^{74} , M. Schiller ID^{57} , H. Schindler ID^{46} , M. Schmelling ID^{18} , B. Schmidt ID^{46} , S. Schmitt ID^{16} , H. Schmitz ID^{73} , O. Schneider ID^{47} , A. Schopper ID^{46} , N. Schulte ID^{17} , S. Schulte ID^{47} , M.H. Schune ID^{13} , R. Schwemmer ID^{46} , G. Schwering ID^{16} , B. Sciascia ID^{25} , A. Sciuccati ID^{46} , S. Sellam ID^{44} , A. Semennikov ID^{41} , M. Senghi Soares ID^{36} , A. Sergi $\text{ID}^{26,m}$, N. Serra $\text{ID}^{48,46}$, L. Sestini ID^{30} , A. Seuthe ID^{17} , Y. Shang ID^6 , D.M. Shangase ID^{79} , M. Shapkin ID^{41} , R.S. Sharma ID^{66} , I. Shchemberov ID^{41} , L. Shchutska ID^{47} , T. Shears ID^{58} , L. Shekhtman ID^{41} , Z. Shen ID^6 , S. Sheng $\text{ID}^{5,7}$, V. Shevchenko ID^{41} , B. Shi ID^7 , E.B. Shields $\text{ID}^{28,o}$, Y. Shimizu ID^{13} , E. Shmanin ID^{41} , R. Shorkin ID^{41} , J.D. Shupperd ID^{66} , R. Silva Coutinho ID^{66} , G. Simi ID^{30} , S. Simone $\text{ID}^{21,h}$, N. Skidmore ID^{60} , R. Skuza ID^{19} , T. Skwarnicki ID^{66} , M.W. Slater ID^{51} , J.C. Smallwood ID^{61} , E. Smith ID^{62} , K. Smith ID^{65} , M. Smith ID^{59} , A. Snoch ID^{35} , L. Soares Lavra ID^{56} , M.D. Sokoloff ID^{63} , F.J.P. Soler ID^{57} , A. Solomin $\text{ID}^{41,52}$, A. Solovev ID^{41} , I. Solovyev ID^{41} , R. Song ID^1 , Y. Song ID^{47} , Y. Song ID^4 , Y.S. Song ID^6 , F.L. Souza De Almeida ID^{66} , B. Souza De Paula ID^3 , E. Spadaro Norella $\text{ID}^{27,n}$,

- E. Spedicato ²², J.G. Speer ¹⁷, E. Spiridenkov⁴¹, P. Spradlin ⁵⁷, V. Sriskaran ⁴⁶, F. Stagni ⁴⁶, M. Stahl ⁴⁶, S. Stahl ⁴⁶, S. Stanislaus ⁶¹, E.N. Stein ⁴⁶, O. Steinkamp ⁴⁸, O. Stenyakin⁴¹, H. Stevens ¹⁷, D. Strekalina ⁴¹, Y. Su ⁷, F. Suljik ⁶¹, J. Sun ²⁹, L. Sun ⁷¹, Y. Sun ⁶⁴, P.N. Swallow ⁵¹, K. Swientek ³⁷, F. Swystun ⁵⁴, A. Szabelski ³⁹, T. Szumlak ³⁷, M. Szymanski ⁴⁶, Y. Tan ⁴, S. Taneja ⁶⁰, M.D. Tat ⁶¹, A. Terentev ⁴⁸, F. Terzuoli ^{32,v}, F. Teubert ⁴⁶, E. Thomas ⁴⁶, D.J.D. Thompson ⁵¹, H. Tilquin ⁵⁹, V. Tisserand ¹¹, S. T'Jampens ¹⁰, M. Tobin ⁵, L. Tomassetti ^{23,k}, G. Tonani ^{27,n,46}, X. Tong ⁶, D. Torres Machado ², L. Toscano ¹⁷, D.Y. Tou ⁴, C. Trippl ⁴², G. Tuci ¹⁹, N. Tuning ³⁵, L.H. Uecker ¹⁹, A. Ukleja ³⁷, D.J. Unverzagt ¹⁹, E. Ursov ⁴¹, A. Usachov ³⁶, A. Ustyuzhanin ⁴¹, U. Uwer ¹⁹, V. Vagnoni ²², A. Valassi ⁴⁶, G. Valenti ²², N. Valls Canudas ⁴², H. Van Hecke ⁶⁵, E. van Herwijnen ⁵⁹, C.B. Van Hulse ^{44,x}, R. Van Laak ⁴⁷, M. van Veghel ³⁵, R. Vazquez Gomez ⁴³, P. Vazquez Regueiro ⁴⁴, C. Vázquez Sierra ⁴⁴, S. Vecchi ²³, J.J. Velthuis ⁵², M. Veltri ^{24,w}, A. Venkateswaran ⁴⁷, M. Vesterinen ⁵⁴, M. Vieites Diaz ⁴⁶, X. Vilasis-Cardona ⁴², E. Vilella Figueras ⁵⁸, A. Villa ²², P. Vincent ¹⁵, F.C. Volle ¹³, D. vom Bruch ¹², V. Vorobyev ⁴¹, N. Voropaev ⁴¹, K. Vos ⁷⁶, G. Vouters¹⁰, C. Vrachas ⁵⁶, J. Walsh ³², E.J. Walton ¹, G. Wan ⁶, C. Wang ¹⁹, G. Wang ⁸, J. Wang ⁶, J. Wang ⁵, J. Wang ⁴, J. Wang ⁷¹, M. Wang ²⁷, N.W. Wang ⁷, R. Wang ⁵², X. Wang ⁶⁹, X.W. Wang ⁵⁹, Y. Wang ⁸, Z. Wang ¹³, Z. Wang ⁴, Z. Wang ⁷, J.A. Ward ^{54,1}, M. Waterlaat ⁴⁶, N.K. Watson ⁵¹, D. Websdale ⁵⁹, Y. Wei ⁶, B.D.C. Westhenry ⁵², D.J. White ⁶⁰, M. Whitehead ⁵⁷, A.R. Wiederhold ⁵⁴, D. Wiedner ¹⁷, G. Wilkinson ⁶¹, M.K. Wilkinson ⁶³, M. Williams ⁶², M.R.J. Williams ⁵⁶, R. Williams ⁵³, F.F. Wilson ⁵⁵, W. Wislicki ³⁹, M. Witek ³⁸, L. Witola ¹⁹, C.P. Wong ⁶⁵, G. Wormser ¹³, S.A. Wotton ⁵³, H. Wu ⁶⁶, J. Wu ⁸, Y. Wu ⁶, K. Wyllie ⁴⁶, S. Xian ⁶⁹, Z. Xiang ⁵, Y. Xie ⁸, A. Xu ³², J. Xu ⁷, L. Xu ⁴, L. Xu ⁴, M. Xu ⁵⁴, Z. Xu ¹¹, Z. Xu ⁷, Z. Xu ⁵, D. Yang ⁴, S. Yang ⁷, X. Yang ⁶, Y. Yang ^{26,m}, Z. Yang ⁶, Z. Yang ⁶⁴, V. Yeroshenko ¹³, H. Yeung ⁶⁰, H. Yin ⁸, C.Y. Yu ⁶, J. Yu ⁶⁸, X. Yuan ⁵, E. Zaffaroni ⁴⁷, M. Zavertyaev ¹⁸, M. Zdybal ³⁸, M. Zeng ⁴, C. Zhang ⁶, D. Zhang ⁸, J. Zhang ⁷, L. Zhang ⁴, S. Zhang ⁶⁸, S. Zhang ⁶, Y. Zhang ⁶, Y.Z. Zhang ⁴, Y. Zhao ¹⁹, A. Zharkova ⁴¹, A. Zhelezov ¹⁹, X.Z. Zheng ⁴, Y. Zheng ⁷, T. Zhou ⁶, X. Zhou ⁸, Y. Zhou ⁷, V. Zhovkovska ⁵⁴, L.Z. Zhu ⁷, X. Zhu ⁴, X. Zhu ⁸, Z. Zhu ⁷, V. Zhukov ^{16,41}, J. Zhuo ⁴⁵, Q. Zou ^{5,7}, D. Zuliani ³⁰, G. Zunică ⁶⁰

¹ School of Physics and Astronomy, Monash University, Melbourne, Australia² Centro Brasileiro de Pesquisas Físicas (CBPF), Rio de Janeiro, Brazil³ Universidade Federal do Rio de Janeiro (UFRJ), Rio de Janeiro, Brazil⁴ Center for High Energy Physics, Tsinghua University, Beijing, China⁵ Institute Of High Energy Physics (IHEP), Beijing, China⁶ School of Physics State Key Laboratory of Nuclear Physics and Technology, Peking University, Beijing, China⁷ University of Chinese Academy of Sciences, Beijing, China⁸ Institute of Particle Physics, Central China Normal University, Wuhan, Hubei, China⁹ Consejo Nacional de Rectores (CONARE), San Jose, Costa Rica¹⁰ Université Savoie Mont Blanc, CNRS, IN2P3-LAPP, Annecy, France¹¹ Université Clermont Auvergne, CNRS/IN2P3, LPC, Clermont-Ferrand, France¹² Aix Marseille Univ, CNRS/IN2P3, CPPM, Marseille, France¹³ Université Paris-Saclay, CNRS/IN2P3, IJCLab, Orsay, France¹⁴ Laboratoire Leprince-Ringuet, CNRS/IN2P3, Ecole Polytechnique, Institut Polytechnique de Paris, Palaiseau, France

- ¹⁵ LPNHE, Sorbonne Université, Paris Diderot Sorbonne Paris Cité, CNRS/IN2P3, Paris, France
¹⁶ I. Physikalisches Institut, RWTH Aachen University, Aachen, Germany
¹⁷ Fakultät Physik, Technische Universität Dortmund, Dortmund, Germany
¹⁸ Max-Planck-Institut für Kernphysik (MPIK), Heidelberg, Germany
¹⁹ Physikalisches Institut, Ruprecht-Karls-Universität Heidelberg, Heidelberg, Germany
²⁰ School of Physics, University College Dublin, Dublin, Ireland
²¹ INFN Sezione di Bari, Bari, Italy
²² INFN Sezione di Bologna, Bologna, Italy
²³ INFN Sezione di Ferrara, Ferrara, Italy
²⁴ INFN Sezione di Firenze, Firenze, Italy
²⁵ INFN Laboratori Nazionali di Frascati, Frascati, Italy
²⁶ INFN Sezione di Genova, Genova, Italy
²⁷ INFN Sezione di Milano, Milano, Italy
²⁸ INFN Sezione di Milano-Bicocca, Milano, Italy
²⁹ INFN Sezione di Cagliari, Monserrato, Italy
³⁰ Università degli Studi di Padova, Università e INFN, Padova, Padova, Italy
³¹ INFN Sezione di Perugia, Perugia, Italy
³² INFN Sezione di Pisa, Pisa, Italy
³³ INFN Sezione di Roma La Sapienza, Roma, Italy
³⁴ INFN Sezione di Roma Tor Vergata, Roma, Italy
³⁵ Nikhef National Institute for Subatomic Physics, Amsterdam, The Netherlands
³⁶ Nikhef National Institute for Subatomic Physics and VU University Amsterdam, Amsterdam, The Netherlands
³⁷ AGH - University of Science and Technology, Faculty of Physics and Applied Computer Science, Kraków, Poland
³⁸ Henryk Niewodniczanski Institute of Nuclear Physics Polish Academy of Sciences, Kraków, Poland
³⁹ National Center for Nuclear Research (NCBJ), Warsaw, Poland
⁴⁰ Horia Hulubei National Institute of Physics and Nuclear Engineering, Bucharest-Magurele, Romania
⁴¹ Affiliated with an institute covered by a cooperation agreement with CERN
⁴² DS4DS, La Salle, Universitat Ramon Llull, Barcelona, Spain
⁴³ ICCUB, Universitat de Barcelona, Barcelona, Spain
⁴⁴ Instituto Galego de Física de Altas Enerxías (IGFAE), Universidade de Santiago de Compostela, Santiago de Compostela, Spain
⁴⁵ Instituto de Física Corpuscular, Centro Mixto Universidad de Valencia - CSIC, Valencia, Spain
⁴⁶ European Organization for Nuclear Research (CERN), Geneva, Switzerland
⁴⁷ Institute of Physics, Ecole Polytechnique Fédérale de Lausanne (EPFL), Lausanne, Switzerland
⁴⁸ Physik-Institut, Universität Zürich, Zürich, Switzerland
⁴⁹ NSC Kharkiv Institute of Physics and Technology (NSC KIPT), Kharkiv, Ukraine
⁵⁰ Institute for Nuclear Research of the National Academy of Sciences (KINR), Kyiv, Ukraine
⁵¹ University of Birmingham, Birmingham, United Kingdom
⁵² H.H. Wills Physics Laboratory, University of Bristol, Bristol, United Kingdom
⁵³ Cavendish Laboratory, University of Cambridge, Cambridge, United Kingdom
⁵⁴ Department of Physics, University of Warwick, Coventry, United Kingdom
⁵⁵ STFC Rutherford Appleton Laboratory, Didcot, United Kingdom
⁵⁶ School of Physics and Astronomy, University of Edinburgh, Edinburgh, United Kingdom
⁵⁷ School of Physics and Astronomy, University of Glasgow, Glasgow, United Kingdom
⁵⁸ Oliver Lodge Laboratory, University of Liverpool, Liverpool, United Kingdom
⁵⁹ Imperial College London, London, United Kingdom
⁶⁰ Department of Physics and Astronomy, University of Manchester, Manchester, United Kingdom
⁶¹ Department of Physics, University of Oxford, Oxford, United Kingdom
⁶² Massachusetts Institute of Technology, Cambridge, MA, United States
⁶³ University of Cincinnati, Cincinnati, OH, United States
⁶⁴ University of Maryland, College Park, MD, United States

- ⁶⁵ Los Alamos National Laboratory (*LANL*), Los Alamos, NM, United States
⁶⁶ Syracuse University, Syracuse, NY, United States
⁶⁷ Pontifícia Universidade Católica do Rio de Janeiro (*PUC-Rio*), Rio de Janeiro, Brazil, associated to³
⁶⁸ School of Physics and Electronics, Hunan University, Changsha City, China, associated to⁸
⁶⁹ Guangdong Provincial Key Laboratory of Nuclear Science, Guangdong-Hong Kong Joint Laboratory of Quantum Matter, Institute of Quantum Matter, South China Normal University, Guangzhou, China, associated to⁴
⁷⁰ Lanzhou University, Lanzhou, China, associated to⁵
⁷¹ School of Physics and Technology, Wuhan University, Wuhan, China, associated to⁴
⁷² Departamento de Física, Universidad Nacional de Colombia, Bogota, Colombia, associated to¹⁵
⁷³ Universität Bonn - Helmholtz-Institut für Strahlen und Kerrphysik, Bonn, Germany, associated to¹⁹
⁷⁴ Eotvos Lorand University, Budapest, Hungary, associated to⁴⁶
⁷⁵ Van Swinderen Institute, University of Groningen, Groningen, The Netherlands, associated to³⁵
⁷⁶ Universiteit Maastricht, Maastricht, The Netherlands, associated to³⁵
⁷⁷ Tadeusz Kosciuszko Cracow University of Technology, Cracow, Poland, associated to³⁸
⁷⁸ Department of Physics and Astronomy, Uppsala University, Uppsala, Sweden, associated to⁵⁷
⁷⁹ University of Michigan, Ann Arbor, MI, United States, associated to⁶⁶
⁸⁰ Département de Physique Nucléaire (*SPhN*), Gif-Sur-Yvette, France

^a Universidade de Brasília, Brasília, Brazil^b Centro Federal de Educacão Tecnológica Celso Suckow da Fonseca, Rio De Janeiro, Brazil^c Hangzhou Institute for Advanced Study, UCAS, Hangzhou, China^d School of Physics and Electronics, Henan University, Kaifeng, China^e LIP6, Sorbonne Université, Paris, France^f Excellence Cluster ORIGINS, Munich, Germany^g Universidad Nacional Autónoma de Honduras, Tegucigalpa, Honduras^h Università di Bari, Bari, Italyⁱ Università di Bologna, Bologna, Italy^j Università di Cagliari, Cagliari, Italy^k Università di Ferrara, Ferrara, Italy^l Università di Firenze, Firenze, Italy^m Università di Genova, Genova, Italyⁿ Università degli Studi di Milano, Milano, Italy^o Università di Milano Bicocca, Milano, Italy^p Università di Padova, Padova, Italy^q Università di Perugia, Perugia, Italy^r Scuola Normale Superiore, Pisa, Italy^s Università di Pisa, Pisa, Italy^t Università della Basilicata, Potenza, Italy^u Università di Roma Tor Vergata, Roma, Italy^v Università di Siena, Siena, Italy^w Università di Urbino, Urbino, Italy^x Universidad de Alcalá, Alcalá de Henares, Spain^y Universidade da Coruña, Coruña, Spain^z Department of Physics/Division of Particle Physics, Lund, Sweden[†] Deceased